12-2017

# Experimental Investigation of Transverse Mode Nozzle Damping

Theron James Price
*University of Tennessee*, tprice11@vols.utk.edu

To the Graduate Council:

I am submitting herewith a thesis written by Theron James Price entitled "Experimental Investigation of Transverse Mode Nozzle Damping." I have examined the final electronic copy of this thesis for form and content and recommend that it be accepted in partial fulfillment of the requirements for the degree of Master of Science, with a major in Aerospace Engineering.

Trevor M. Moeller, Major Professor

We have read this thesis and recommend its acceptance:

John D. Schmisseur, L. Montgomery Smith

Accepted for the Council:
Dixie L. Thompson

Vice Provost and Dean of the Graduate School

(Original signatures are on file with official student records.)

# Experimental Investigation of Transverse Mode Nozzle Damping

A Thesis Presented for the

Master of Science

Degree

The University of Tennessee, Knoxville

Theron James Price

December 2017

# ACKNOWLEDGEMENTS

This thesis is the product of labor of many individuals, without whom much of this work would have been impossible. Mere words of thanks are hardly any consolation for the hours of effort spent in this project, but I must express my sincerest gratitude to all individuals who assisted me in this effort.

I express my gratitude towards my advisor, Dr. Trevor M. Moeller, for hiring me as a graduate research assistant, and assisting me in choosing this thesis topic. I also extend my gratitude to Dr. Eric J Jacob and Dr. Joshua W. Batterson of Gloyer-Taylor-Laboratories for the extensive technical advice they provided over the course of this work. A very special thanks must be extended to Jake Cranford, of GTL, for similarly providing fantastic technical support in response to my many pestering emails littered with thousands of questions, as well as providing numerous useful anecdotes about his time as a Masters candidate.

I am forever indebted to Jonathan Kolwyck and Andrew Davis of the University of Tennessee Space Institute's (UTSI) Technical Research Support Group (TSRG) for going far, *far* beyond the call of duty in assisting me with the technical side of this project, and for teaching a novice engineer the right way to hold a wrench, among many other technical aspects that cannot be learned in classroom. In many ways, this project was more than a one-man job, and I could always count on them when I needed help. I must also express my sincere thanks and respect to Jack LeGeune and Gary Payne of UTSI for the masterful machining work performed on the nozzles, and for dealing with a novice's attempts at producing engineering drawings.

I would like to extend my appreciation towards Dr. John D. Schmisseur and Dr. L. Montgomery Smith for serving on my committee, and for dealing with my unnecessary verbosity in print. I also extend my thanks to my friends at UTSI, for putting up with my at-times disagreeable personality and absentminded nature over the course of this work. Special thanks must be given to Stefen Lindörfer, whom supplied me with much advice about this entire process, and continually reminded me of deadlines I would have otherwise forgotten.

Finally, I must extend my most heartfelt thanks and respect for my mother, Donna J. Price, for raising my sister and I through many difficult years. Her patience, understanding, and optimism are things I can only dream of possessing one day, and without her guidance I would not be the man I am today. There are no words in any language sufficient to express my gratitude for the years of support, advice, and love she has given me.

Thank you, all of you.

# ABSTRACT

Combustion instability remains one of the most stifling problems in the design of propulsive technologies. Instabilities may emerge as a result of a feedback mechanism between unsteady heat release and the acoustic modes of the combustion chamber, and these instabilities often have the potential to seriously damage, or even destroy, the vehicle experiencing these oscillations. To address underrepresentation in the literature involving transverse mode nozzle damping relative to longitudinal damping, an experimental campaign involving three nearly-identical nozzles was conducted at the University of Tennessee Space Institute. The goals of this experiment were to produce data corresponding to the attenuation of excited transverse modes within the nozzles, and to use this data to determine an ideal nozzle geometry for each mode. The geometry of the nozzles differed only at the convergent sections, and this identifying characteristic was used to label the nozzles as follows: an equal-radius-of-curvature (ER) nozzle, a conical nozzle, and a linear-velocity-profile (LVP) nozzle.

Excitation was provided by a frequency-variable, pneumatic siren, and attenuation was facilitated by a spring activated, 3D printed gate-valve placed at the outer wall of the chambers. The pneumatic siren injected oscillatory flow from the sidewall of the chambers, and could reliably operate from 1500 to 2000 Hz. The decay of the modes were measured by six pressure transducers arranged in either a tangential array or a mixed tangential-longitudinal array, and an exponential decay rate, $\alpha$, was computed from the data collected at various locations within the nozzle by applying a linear fit to the natural logarithm of the upper envelope of the pressure traces. This thesis presents data on the first tangential (1T) mode in all three nozzles. In general, it was observed that the ER nozzle provides the most 1T damping, followed by the conical nozzle, which is followed by the LVP nozzle. The methodology described herein is easily applicable to other modes and geometries.

# TABLE OF CONTENTS

# LIST OF TABLES

# LIST OF FIGURES

# NOMENCLATURE

## Uppercase Letters:

| | | |
|---|---|---|
| *A-H* | - | arbitrary constants |
| *C* | - | conical nozzle |
| *ER* | - | equal-radius-of-curvature nozzle |
| *F(t)* | - | force |
| *HFI* | - | high frequency instability |
| *IFI* | - | intermediate frequency instability |
| $J_m$ | - | mth order Bessel function of the first kind |
| *L* | - | length |
| *LRE* | - | liquid rocket engine |
| *LVP* | - | linear-velocity-profile nozzle |
| *N* | - | number of periods |
| *M* | - | Mach number |
| *P* | - | pressure |
| $\hat{P}$ | - | time-dependent acoustic amplitude |
| *Re* | - | Real |
| ***R(r)*** | - | radial component of the wave equation |
| *SRM* | - | solid rocket motor |
| ***T(t)*** | - | time component of the wave equation |
| *U* | - | velocity |
| *Y* | - | nozzle admittance |
| $Y_m$ | - | mth order Bessel function of the second kind |
| ***Z(z)*** | - | azimuthal component of the wave equation |

## Lowercase Letters:

| | | |
|---|---|---|
| *a* | - | sonic speed |
| *b* | - | damping coefficient |
| *f* | - | frequency, hz |
| *k* | - | restoring force coefficient; spring constant |

| | | |
|---|---|---|
| $l$ | - | longitudinal mode number |
| $m$ | - | tangential mode number |
| $m_{body}$ | - | mass |
| $r$ | - | radial distance |
| $u$ | - | arbitrary vector property (e.g., velocity) |
| $x$ | - | position |
| $z$ | - | azimuthal distance |

## Greek Letters:

| | | |
|---|---|---|
| $\boldsymbol{\Theta(\theta)}$ | - | tangential component of the wave equation |
| $\alpha$ | - | decay rate |
| $\gamma,\lambda,\nu$ | - | substitution factors |
| $\alpha_{mn}$ | - | nth root of the first derivative of the mth order Bessel function of the first kind |
| $\xi$ | - | damping ratio |
| $\rho$ | - | density |
| $\omega$ | - | angular frequency, rad/s |

## Subscripts:

| | | |
|---|---|---|
| $0$ | - | reference condition |
| $\theta,r,t,z$ | - | derivative with respect to the tangential, radial, temporal, or azimuthal variable |
| $N$ | - | nozzle-specific quantity |
| $c$ | - | combustion chamber, or combustor, specific quantity |
| $m,n,l$ | - | mode-number subscripts |
| $p$ | - | perturbation quantity |

# CHAPTER ONE
# INTRODUCTION

The objective of the present work may be broadly summed as an experimental investigation into the damping behavior of nozzles connected to equivalent combustion chambers. The configurations of the convergent portion of the nozzles differ and are based on configurations from earlier studies **[1, 2]**. Specifically, the convergent sections are: one conical section; one equal-radii-of-curvature section; and one section that, based on purely isentropic theory, produces a linearly increasing velocity profile. Henceforth, these nozzles were referred to as, respectively, the conical, equal-radii-of-curvature (ER), and linear velocity profile (LVP) nozzles. Previous experiments focusing on longitudinal mode oscillations have demonstrated that the conical nozzle most strongly damps out axial oscillations, followed by the ER nozzle, which is trailed by the LVP nozzle **[1, 2]**.

## 1.1 Combustion Instability

Combustion instabilities are present in all forms of propulsion dependent upon the combustion of some reacting medium for thrust production. In particular, combustion instabilities have plagued the development and flight of all forms of rocket engines from their inception, and remain one of the most significant issues to be surmounted in the field of rocketry. Even the prediction of instabilities occurring in combustion chambers is a significant challenge to the development of modern propulsion technologies **[3, 4]**, to the point that mitigation efforts are often mired by the application of *ad hoc* solutions that succeeded in the past under different conditions and have no guarantee of success for the current system in question **[5]**. As such, there is much empiricism involved when designing for stability—or when addressing observed instabilities—that exacerbates development cost and time **[6]**.

Most instabilities in combustion are primarily characterized by strong oscillatory pressure fluctuations both spatially and temporally—that is, in a system containing instabilities, the pressure at a particular location within the system will differ from another

point within the system, and pressure at all points changes with time. The magnitude of the differences in pressure depends upon the degree and overall behavior of the present oscillations—weak perturbations that are not permitted to grow beyond a certain threshold may only slightly induce pressure fluctuations, while strong perturbations may introduce high pressure fluctuations. The analysis of combustion instabilities quickly becomes a question of how energy is distributed throughout a system, and the magnitude of the gains and losses of energy **[2, 7-11]**. Figure 1.1 depicts a simple energy balance of a typical rocket combustion chamber. Vortex shedding and boundary layer pumping arise from behavior of the fluid within the chamber, whereas propellant burning response and distributed combustion emerge as combustion phenomena. Viscous losses and flow-turning are possible loss terms tied to the fluid dynamics of the motor, and particle damping depends on the presence of additive particles in the flow which can break up acoustic waves—aluminum particles are a common example in solid rockets. Nozzle damping is a loss term dealing primarily with the design of the attached nozzle and its interaction with the fluid system in the combustion chamber.

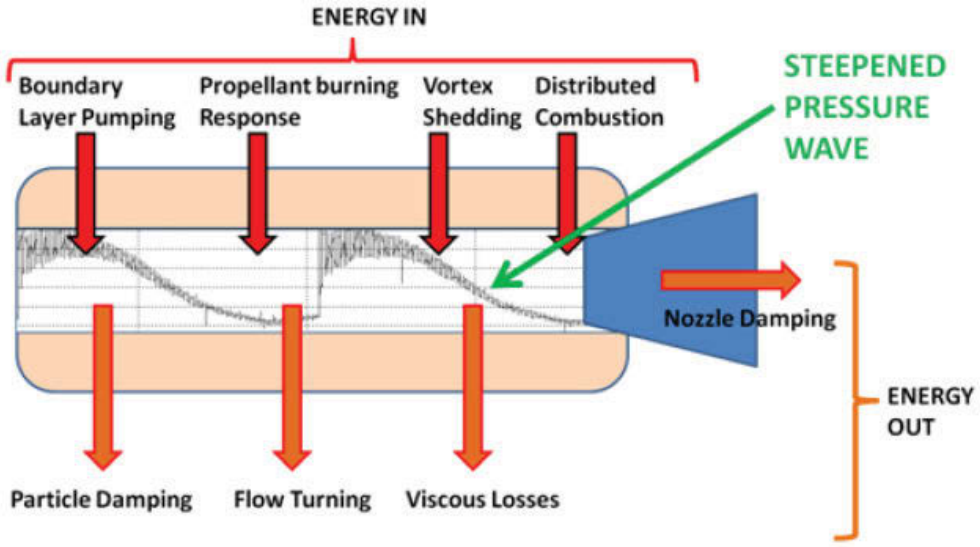


**Figure 1.1.** Energy Balance of a Simple Combustion Chamber **[7]**

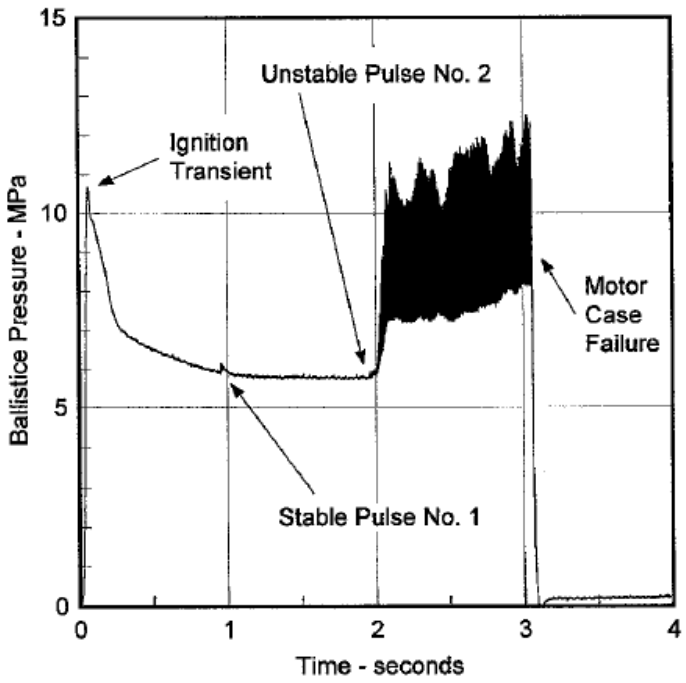


**Figure 1.2**. Example of an Unstable Pressure Trace from a Solid Rocket Motor **[12]**

The behavior of the energy sources and sinks—and thus the behavior of the instabilities present—depend largely upon the boundary conditions of the system in question **[13]**, which are usually not constant across configurations. Regardless of configuration, the implications of the energy balance are immediately obvious: if the gains in energy exceed the magnitude of losses in energy within the system, then system energy will build in the form of increasing pressure until some form of pressure relief is triggered, and more often than not this is accomplished through catastrophic failure of the rocket casing. An example of such an unmitigated rise in pressure until motor failure is presented in Figure 1.2, where the internal instability was triggered intentionally by a shock-tube connected to the motor **[12]**.

### *1.1.1 An Historical Example of Combustion Instability*

Before introducing a more technical discussion of combustion instability, it is prudent to introduce a real-world example of instability. This example will assist in

characterizing the complex nature of combustion instability. The most widely known—and most often quoted—example of combustion instability involves the Rocketdyne F-1 engine. The development period of the F-1 engine spanned the mid-1950's to the early 1970's, with the intent to develop a liquid rocket engine (LRE) sufficient for the heavy-lift requirements of the Apollo program **[14]**.

The F-1 engine suffered initially from high-frequency, high-amplitude oscillations on the order of 3.5 MPa relative to the mean combustion pressure of 7.8 MPa. Much of the instability mitigation effort focused on redesigning the injector face through which propellant was atomized, and mixed downstream **[14]**. Baffled injectors were found to exhibit a stabilizing influence through three means: modification of the internal acoustics of the combustion chamber; modification or restriction of oscillatory flow patterns by the presence of baffles; and the provision of damping mechanisms to oscillations by flow effects induced (e.g., vortices) by the baffles. The final design of the F-1 managed to attenuate high-frequency oscillations to what was considered acceptable **[14]**, and history speaks of the success of the development cycle through the success of the Saturn V.

### *1.1.2 Characteristics of Instabilities*

Many important characteristics of instabilities are revealed through the development of the F-1 engine. The first being that even if the growth of oscillations is controlled or insufficient to drive an immediate structural failure, existing oscillations of pressure in the system may be so severe such that stable or prolonged flight would be impossible. Figure 1.3 depicts a typical pressure trace of early testing of the F-1 engine, in which pressure oscillations were a significant percentage of the mean. Such high-frequency pressure oscillations of that magnitude can be destructive to a structure or material that is without significant reinforcement. Even supposing a vibration-resilient structure, the non-uniform pressure may introduce localized regions of increased heating **[15]** that could similarly induce a structural failure.

Another characteristic of instabilities is that the driving phenomena behind the pressure fluctuations tends to couple with random noise or pressure pulses **[7]**. When

intentionally inducing these sources of noise, a common test is to set off an explosive charge—as was done during testing of the F-1—or utilize some other pressure pulsing device—as was used in reference **[12]**. A stable motor would then, over some span of time, attenuate the pressure oscillations driven from this pulsing. Conversely, an unstable system would encourage the growth of these oscillations **[7]**.

Perhaps the most important characteristic revealed by the F-1 engine tests, however, is dependency of oscillations on the *acoustic* properties of the system—in this case, the combustion chamber. The baffle designs that were most successful were those that influenced the frequency of oscillation of the unstable mode in question **[14]**. Such is the importance of the acoustics of a rocket chamber that, when discussing instabilities, the terms thermo-acoustic instabilities or, simply, acoustic instabilities are more descriptive. Indeed, the very term *combustion* instability is actually misleading **[7]**. Oscillatory behavior can be driven without combustion, provided that sufficient energy is added to the system to induce the motion of air. Combustion provides this energy through the inherent release of heat and increase in pressure—both of which induces convection. However, there are other well-documented means of exciting geometries without combustion—some examples of cylindrical geometries, which represent typical combustion chambers, include the excitation of a clarinet or similar instrument by an application of pressure, or the excitation of a Rijke tube by a heating element **[16]**. Should some percentage of the driving energy manage to couple with the natural frequencies of the geometry, the result is far

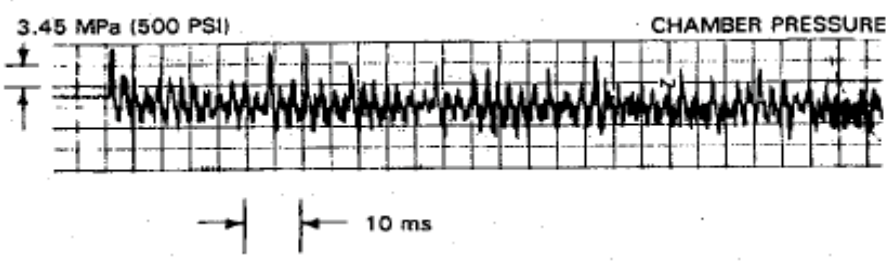


**Figure 1.3.** Typical Pressure Trace of Early F-1Engine Testing **[14]**

stronger amplitudes of oscillation via resonance **[7]**. Acoustic instability will be examined in greater detail in a later chapter—for now it is sufficient to simply note that acoustics are a major driver of instabilities in rocket engines.

## 1.2 Overview of Nozzle Damping

Referring back to Figure 1.1, the phenomenon termed "nozzle damping" is listed as an energy sink, along with particle damping, flow turning, and viscous losses. Nozzle damping refers to the physical convection of acoustic energy out of the system through the nozzle, and—relative to other sources of energy loss—is the principle damping source in most rocket motor or engine configurations **[10, 17-20]**. Ideally, a rocket nozzle should be designed to possess significant nozzle damping in order to suppress the growth of potential instabilities well before they can propagate. In practice, however, other performance specifications must be heeded when designing a nozzle. Experimental results in the past have shown that solid rocket motor (SRM) combustion chambers are more conservative—that is, more retentive of acoustic energy—as the difference between throat area and grain port area increases **[11, 21]**. In other words, a strongly convergent nozzle design built to induce a high exit velocity and thrust may not adequately damp out instabilities. Such a nozzle possesses both a greater surface area with which to reflect acoustic waves, and possesses a reduced mass flux through which acoustic waves may propagate. However, this example does illustrate that stability and high-performance may be at odds within the confines of nozzle design.

Nozzle damping and all other sources of energy loss are intimately tied to the geometrical boundaries of a system such that is insufficient to perform an acoustic analysis on an isolated nozzle **[13]**. Even in subscale, cold-flow experiments it is necessary for an adjoining combustion chamber model to be present. Such experimental studies often focus on determining a factor known as the *admittance* of a nozzle, the value of which influences the nature and magnitude of acoustic loss through said nozzle **[22]**. Several experimental methods exist for determining this parameter—a more detailed discussion will be presented in a later chapter.

However, other experimental means exist for determining the magnitude of nozzle damping for a given oscillatory mode. By applying linear stability theory, the stability of a motor or engine can be characterized by equation **(1.1)**, where $\hat{P}$ is the acoustic wave amplitude, $P_o$ is the initial amplitude of the wave, $\alpha$ is the rate of change for the energy in the system, and $t$ represents time **[18, 23]**.

$$\hat{P}(t) = P_o \exp(\alpha t) \tag{1.1}$$

The sign of $\alpha$ determines the behavior of the system. In this definition, for $\alpha$ less than zero the system is defined as unstable, and for $\alpha$ greater than zero the system is defined as stable. An observation can be made regarding the behavior of this model as time approaches infinity for a positive rate of change: There is no limiting parameter such that oscillations are permitted to grow unbounded. In reality, non-linear effects intercede and the acoustic amplitude approaches a finite amplitude limit cycle **[5]**. As such it must be noted that the linear model has limited use beyond an initial approximation of acoustic growth, as it cannot possibly predict long-term behavior in a system. However, in the case of acoustic decay, this linear model finds itself well applied such that nozzle decay coefficients based on $\alpha$ have been determined **[20]**. The present study will be primarily concerned with an examination of nozzle damping through this method, though—for reasons to be later explicated—it may be more apt to refer to the observed damping as total system damping rather than purely nozzle damping.

## 1.3 Objective

The overarching objective of these studies was to investigate the damping trend of these nozzles under transverse mode excitation, in order to address an underrepresentation in the literature on transverse mode damping. For all experimental investigations, the following variables were kept approximately constant to improve repeatability and engender better comparison:

- Combustion chamber length and diameter
- Length of the convergent section in the nozzles
- Contour and length of the divergent section in the nozzles

- Throat diameter and location within the nozzles
- Pressure of the acoustic excitation source
- Actuation time of the gate-valve that isolates the chambers from the acoustic excitations from the siren

The scope of this work was initially larger, involving proposed studies into longitudinal, transverse, and mixed longitudinal-transverse mode excitation under both no-mean flow and mean flow conditions. Specifically, the 1L, the 1T, and the 1T1L modes were of most initial interest. However, several factors colluded to preclude mean-flow excitation in general, and only 1T and 1T1L data were taken under no-mean flow conditions. Of these experiments, only the 1T yielded clean data.

Chapter II presents an introduction to acoustics and its extension to combustion instability studies, and also presents a discussion of longitudinal and transverse modes. Chapter III provides a discussion on nozzle damping including both theory and experimental methods used to evaluate this loss mechanism. Chapter IV outlines the experimental approach and setup, including details of the instrumentation and all salient features that influence the collected results. Test geometry specifications are provided, and the means of inducing the acoustic attenuation of an excited mode is discussed. Chapter V discusses the details of the numerical analysis techniques employed over the course of this investigation. Chapter VI presents the results of these investigations. Chapter VII concludes this thesis, and consists of relevant conclusions gained from the experiments. A summary and ideas for future work are incorporated.

# CHAPTER TWO
# ACOUSTICS

## 2.1 Introduction

Acoustics is primarily the study of mechanical waves and the vibrations that are thus associated. As applied to combustion instability, acoustics can aid in identifying the natural resonant frequencies that exist in a given geometry which may become unstable. This is because waves of various types—when confined in an arbitrary cavity as opposed to freely radiating—are defined uniquely by their boundary conditions **[13]**. The existence of a waveform is made possible at the particle-level, where individual particles of a constituent material are perturbed by some initial input of energy. Dependent upon the physical state and density of the medium, this energy is transferred at some rate by the collisions of these vibrating particles **[24]**. Sustained wave-motion is then the combined oscillatory motion of a continuum of particles that forms a medium **[25]**, and hence it useful to begin a discussion of acoustic with particle vibrations.

### *2.1.1 Particle Vibrations*

Randall's *An Introduction to Acoustics* **[26]** provides a useful introduction to particle vibration modeled by simple harmonic motion. There are numerous assumptions at play when referring to this model—principal among them that the overall behavior of the oscillations is *linear*. Linear models—simple harmonic motion or otherwise—are accurate only for increasingly small perturbations **[24]** not present when dealing with real (or non-ideal) fluids **[7]**. The presence of combustion—with the resultant unsteady energy transport through the system—further detracts from the accuracy of linear models. However, linear models still provide a useful base upon which to first approach the issue of instabilities.

For damped, simple harmonic motion, the following familiar equation applies, where $m_{body}$ refers the mass of the oscillating body, $b$ refers to some damping influence on the oscillating body, and $k$ is an elastic restoring force.

$$m_{body}\ddot{x} + b\dot{x} + kx = F(t) \quad \textbf{(2.1)}$$

The oscillatory nature of the unforced solution of equation **(2.1)** is well-known. The frequency-dependent nature is revealed after two substitutions, which leads to equation **(2.4)**.

$$\omega_0 = \sqrt{k/m_{body}} \quad \textbf{(2.2)}$$

$$\xi = b/(2\sqrt{km_{body}}) \quad \textbf{(2.3)}$$

$$\ddot{x} + 2\xi\omega_0\dot{x} + \omega_0^2 x = F(t) \quad \textbf{(2.4)}$$

Here, $\omega_o$ is defined as the angular frequency of the system, and $\xi$ is defined as the damping ratio. For the unforced system, three distinct cases based on the damping ratio are possible. It can readily be shown that the nature of the discriminant, which in turn influences the nature of the roots of the system, depends entirely on the value of the damping coefficient for constant frequencies between cases **[27-29]**.

- For $\xi < 1$, there are two complex conjugate roots to the characteristic equation. This case is defined as *underdamped*.
- For $\xi = 1$, there is one real, repeated root to the characteristic equation. This case is defined as *critically damped*.
- For $\xi > 1$, there are two distinct, real roots to the characteristic equation. This case is defined as *overdamped*.

These three terms collectively refer to the influence of damping on the oscillatory nature of the system—underdamped systems are so called because the damping isn't strong enough to terminate oscillation; critically damped and overdamped systems do not oscillate, as damping was exactly sufficient and stronger than necessary, respectively **[27]**. While acoustic waves typically attenuate by one of the three listed behaviors in time and space **[25]**, underdamped oscillations will be the focus of this investigation. Physically, this is so due to the reflection of incident acoustic waves inside the combustion chamber at the nozzle throat—while some energy is indeed lost out of the nozzle, the reflected waves still retain their properties at a reduced amplitude and different phase, and this process

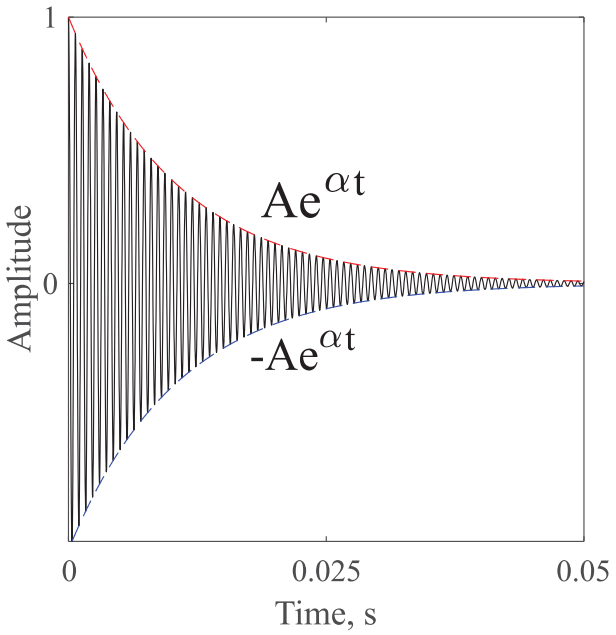


**Figure 2.1.** Underdamped Oscillatory Motion

continues until all or most of the energy is finally lost. If all acoustic energy were able to be vented within one cycle, the behavior may more closely approximate the critically or overdamped cases.

The key to analyzing underdamped systems is knowing that the attenuating signal is bounded by two functions: an exponentially decaying function—$Ae^{\alpha t}$—and the negative thereof, where α is an arbitrary number less than zero for decaying systems, and A is an arbitrary initial amplitude. Figure 2.1 illustrates this for a generic decaying sinusoid with an angular frequency of 100 radians per second, or roughly 16 Hz. Being able to either find experimentally or compute numerically a value of α is invaluable when considering linear growth or decay rates, and this process is a core component of the data analysis described in Chapter V, which will be centered on analyzing the decay over time of frequency-specific data. For the generic example posed in Figure 2.1, and using the notation prescribed by equation **(2.4)**, it follows that alpha is equal to the damping ratio multiplied by the angular frequency—in other words, the real component of the complex roots.

### *2.1.2 Waves*

The displacement by any means of a portion of an extended, cohesive medium brings about wave motion. Under a set of restrictive assumptions, the variation of a general property $u$ both temporally and spatially can be prescribed as the familiar result:

$$u_{tt} = a^2 \nabla^2 u \qquad \textbf{(2.5)}$$

This is the well-known wave equation, with derivations provided in a number of sources **[7, 24-27]**. The assumptions necessary to reach this result for any gas-dynamic system are as follows:

1. The system is isentropic.
2. The system is thermally perfect—that is, the gas does not chemically react and enthalpy is a function of temperature only.
3. The displacements, or perturbations, *are always small* such that disturbances to state variable are negligible. **[24, 26]**

With these assumptions made, pressure, $p$, can be substituted in for the variable $u$. Mathematically, the third assumption is not necessary—this wave equation will predict the same type of behavior for a variety of amplitudes. Rather, the third assumption is a restriction required by reality—that is, for high amplitude displacements, predicted and actual behaviors begin to diverge, and wave-steepening can begin to dominate the periodic structure of the wave **[7, 24]**. Physically, this is observed because the local speed of propagation for the wave is no longer constant when disturbances are of sufficient magnitude. Different wave-structures emerge as the entire wave is no longer uniform in rate of travel—the compression shock that occurs as one wavefront intercepts a slower wavefront is one example **[24, 25]**. In the presence of combustion, all three assumptions are violated, but the violation of the third assumption has the largest impact on the degree of error introduced by equation **(2.5)**. There exist other forms of the wave equation that attempt to rectify the errors of the simpler form, ranging from forms that include the effect of compressibility and the variation of velocity thereof, to those that incorporate the influence of damping and energy loss. Such forms are beyond the scope of this work, and the present discussion will continue to employ the simple form observed in equation **(2.5)**.

True to the nature of waves, there are frequencies associated with the various modes predicted by the wave equation. These frequencies are dependent upon the prescribed boundary conditions of the problem—for example, a closed-closed tube will have a different fundamental frequency than a closed-open tube. It can readily be shown that, for the closed-closed, one-dimensional case the expression for the longitudinal frequency, $\omega_l$, is:

$$\omega_l = \frac{l\pi a}{L} \tag{2.6}$$

Here, $l$ is defined as an element of the natural numbers, $a$ is the mean speed of sound in the tube, and $L$ is the total length of the tube. As much of the literature involving nozzle damping touches upon the longitudinal mode, this is a useful expression to keep in mind for purposes of the present work. However, there are more modes of oscillation that exist and influence the stability of rocket chambers—namely, transverse modes, which arise from the three-dimensional nature of the problem. To that end, it is necessary to investigate oscillating modes in a three-dimensional perspective. The solution of the wave equation for a three-dimensional cylindrical geometry is less prevalent in the literature, and so for convenience salient details are provided below. The derivation is facilitated by assuming a product solution and applying separation of variables **[30]**. It can be shown that the Laplacian of the general variable $u$ in cylindrical coordinates is:

$$\nabla^2 u = \frac{1}{r}u_r + u_{rr} + \frac{1}{r^2}u_{\theta\theta} + u_{zz} \tag{2.7}$$

A product solution of $u$ is assumed such that:

$$u = \boldsymbol{R}(r)\boldsymbol{\Theta}(\theta)\boldsymbol{Z}(z)\boldsymbol{T}(t) \tag{2.8}$$

$$\boldsymbol{R\Theta Z T}_{tt} = a^2[\frac{1}{r}\boldsymbol{\Theta Z T R}_r + \boldsymbol{\Theta Z T R}_{rr} + \frac{1}{r^2}\boldsymbol{R Z T \Theta}_{\theta\theta} + \boldsymbol{R\Theta T Z}_{zz}] \tag{2.9}$$

Dividing all terms by the common $u$, rearranging the position of the speed of propagation, and setting the results equal to an arbitrary constant yields:

$$\frac{1}{a^2}\frac{\boldsymbol{T}_{tt}}{\boldsymbol{T}} = \frac{1}{r}\frac{\boldsymbol{R}_r}{\boldsymbol{R}} + \frac{\boldsymbol{R}_{rr}}{\boldsymbol{R}} + \frac{1}{r^2}\frac{\boldsymbol{\Theta}_{\theta\theta}}{\boldsymbol{\Theta}} + \frac{\boldsymbol{Z}_{zz}}{\boldsymbol{Z}} = -\lambda^2 \tag{2.10}$$

The solution to the temporal portion of the differential equation is the familiar harmonic oscillator:

$$\boldsymbol{T}(t) = A\cos(a\lambda t) + B\sin(a\lambda t) \tag{2.11}$$

In fact, of the remaining three independent solutions, only the radial solution will assume a form other than the harmonic oscillator. Continuing with the separation of variables, a substitution factor $-\gamma^2$ is introduced for the radial and angular components such that:

$$-\gamma^2 = \frac{1}{\boldsymbol{R}}\left(\frac{1}{r}\boldsymbol{R}_r + \boldsymbol{R}_{rr}\right) + \frac{1}{r^2}\frac{\boldsymbol{\Theta}_{\theta\theta}}{\boldsymbol{\Theta}} \tag{2.12}$$

$$-\gamma^2 + \frac{\boldsymbol{Z}_{zz}}{\boldsymbol{Z}} = -\lambda^2 \tag{2.13}$$

Solving for $\boldsymbol{Z}$ follows the same procedure as for the time-based solution and other such harmonic oscillators. Given that, in the absence of all other dimensions or variables, this solution should represent the 1-D longitudinal solution of the wave equation should not be surprising. It then follows that:

$$\boldsymbol{Z}(z) = C\cos(z\sqrt{\lambda^2 - \gamma^2}) + D\sin(z\sqrt{\lambda^2 - \gamma^2}) \tag{2.14}$$

Returning to equation **(2.12)**, multiplying by $r^2$ to simplify the angular term, setting the result equal to an arbitrary constant $v^2$, and separating the angular term from the radial yields the following result:

$$-\frac{\boldsymbol{\Theta}_{\theta\theta}}{\boldsymbol{\Theta}} = \frac{r^2}{\boldsymbol{R}}\left(\boldsymbol{R}_{rr} + \frac{1}{r}\boldsymbol{R}_r\right) + r^2\gamma^2 = v^2 \tag{2.15}$$

Solving for the angular solution is trivial.

$$\boldsymbol{\Theta}(\theta) = E\cos(v\theta) + F\sin(v\theta) \tag{2.16}$$

The radial solution may be rearranged to form a parametric form of Bessel's Equation, with solutions known to comprise Bessel functions of the first and second kind.

$$r^2\boldsymbol{R}_{rr} + r\boldsymbol{R}_r + (\gamma^2 r^2 - v^2)\boldsymbol{R} = 0 \tag{2.17}$$

$$\boldsymbol{R}(r) = GJ_v(\gamma r) + HY_v(\gamma r) \tag{2.18}$$

In equations **(2.11)** through **(2.18)**, the letters A through H represent arbitrary constants; the values thereof depending on the boundary conditions, which are now introduced. A closed-closed cylinder with impenetrable walls is supposed, and continuity from 0 to 2π in the radial direction is enforced. The impenetrable walls require that values at the wall vanish—i.e., there is no flow through the boundary of the tube. The final boundary conditions required for a meaningful physical solution are that, along the outer

walls of the tube—i.e., $r = r_o$—a bounded solution of $\boldsymbol{R}$ is required, and $\boldsymbol{R}_r$ is zero. It can then be readily shown that constants $C$ and $H$ immediately reduce to zero, and that equation **(2.16)** is true if and only if $v$ is equal to successive integer values from 0 to infinity. That is:

$$v = m \; \forall \; m \in \mathbb{N}, or \; m = 0,1,2,3 \ldots \tag{2.19}$$

This infinite series is represented by $m$ arbitrarily. Since the derivative of the radial solution at $r = r_o$ is enforced, it must follow that values of $\gamma r_o$ are equal to the roots of the first derivative of the Bessel function, $J_m$, where the substitution $v = m$ has been made, and the trivial solution of $F = 0$ is not permitted.

$$J'_m(\gamma r_o) = 0 \tag{2.20}$$

$$\gamma_{mn} = \frac{\alpha_{mn}}{r_o}, m \in \mathbb{N}, n \in \mathbb{N} \tag{2.21}$$

Returning the solution of $\boldsymbol{Z}$, where only the sine term remains, enforcing again the impenetrable wall boundary condition requires that $\boldsymbol{Z}(0) = \boldsymbol{Z}(L)$, and by neglecting the trivial solution of $D = 0$, it follows that this condition is held if and only if the argument of the sine function reduces to integer multiples of pi. Thus, at L:

$$L\sqrt{\lambda^2 - \gamma_{mn}^2} = l\pi, l \in \mathbb{N} \tag{2.22}$$

Solving for $\lambda$ yields:

$$\lambda_{mnl} = \sqrt{\gamma_{mn}^2 + \left(\frac{l\pi}{L}\right)^2} = \sqrt{\left(\frac{\alpha_{mn}}{r_o}\right)^2 + \left(\frac{l\pi}{L}\right)^2} \tag{2.23}$$

Finally, the solution can be summarized as thus:

$$\omega_{mnl} = a\lambda_{mnl} = a\sqrt{\left(\frac{\alpha_{mn}}{r_o}\right)^2 + \left(\frac{l\pi}{L}\right)^2} \tag{2.24}$$

$$\begin{aligned} u(r,\theta,z,t) = \sum_{m=0}^{\infty}\sum_{n=0}^{\infty}\sum_{l=0}^{\infty} \begin{pmatrix} A_{mnl}cos(\omega_{mnl}t) \\ B_{mnl}\sin(\omega_{mnl}t) \end{pmatrix} \begin{pmatrix} \cos(m\theta) \\ \sin(m\theta) \end{pmatrix} \\ * \cos(z\sqrt{(\lambda_{mnl}^2 - \gamma_{mn}^2)}(J_m(\gamma_{mn}r))) \end{aligned} \tag{2.25}$$

Equation **(2.25)** provides the *full* solution of the three-dimensional wave equation, in which all mode shapes—designated by the values of m, n, and l—are present. Individual mode shapes are characterized by solutions for specific values of m, n, and l. In general, the following is true:

- For nonzero values of m, and zero values of n and l, the mode is deemed *tangential*.
- For nonzero values of n, and zero values of m and l, the mode is deemed *radial*.
- For nonzero values of l, and zero values of m and n, the mode is deemed *longitudinal* **[31]**.

This last point is easily verified by substituting the appropriate values into equation **(2.24)**, and by observing that it reduces to equation **(2.6)**—the equation for the frequency of a one-dimensional, longitudinal wave. Mixed modes are also possible, where there exist multiple nonzero subscripts. Notation takes the form "mT nR lL", where "T" refers to tangential, "R" refers to radial, and "L" refers to longitudinal. Zero subscripts are omitted, so a mixed tangential and longitudinal mode defined by their first resonant frequencies would be known as the 1T1L mode **[32]**.

Note that equation **(2.25)** is restricted by the same set of assumptions that limited the wave equation. Further, there is no treatment of wave attenuation within the framework of said equation, and thus a work principally concerned with damping finds little use for equation **(2.25)**. Moreover, Equation **(2.25)** is applicable only for cylinders of fixed geometry—the introduction of convergent and divergent sections greatly adds additional complexity with regards to compressibility. However, equation **(2.24)** is of much greater use insofar as it serves as a quick-to-evaluate equation for predicting longitudinal, transverse, and mixed modes of oscillation—each of which can be a potential stability problem. Further, the constant geometry restriction, while present in equation **(2.24)**, may still be applied to slightly more complicated geometries provided the experimental method is able to determine the *actual* frequencies of the various modes of oscillation **[33]**. In other words, the experiment provides a measured frequency, and equation **(2.24)**—the result of which will be different depending on the conditions of the experiment (e.g. combustion,

variable geometry, etc.) provides the characteristic of the mode. The experimental method used in the present work is capable of just that, and will be detailed in Chapter IV.

## 2.2 Acoustic Instability

The problem of *acoustic* instability has been summarized repeatedly as a phenomenon owing to the coupling between unsteady heat release from combustion and the natural acoustic modes of the combustor **[3, 4, 7, 8, 11, 18, 21, 34-38]**, and is one of many participating elements in the overall picture of combustion instability **[5, 14, 31]**. In general, the development of an acoustic instability may be envisioned as follows:

1. An oscillatory mode in the combustion chamber is excited by some phenomenon, with the preeminent example being the energy released during combustion. This excitation may either be self-excited or driven **[7, 39]**.
2. This acoustic mode influences the gas dynamics of the chamber by introducing wave motion in velocity and pressure.
3. This wave motion impinges at the combustion source, and influences the boundary conditions of combustion primarily through pressure (and temperature).
4. The burning process is influenced by the oscillatory pressure, and develops an oscillatory response to these conditions.
5. This oscillatory response may either add to or subtract from the acoustic energy of the system depending on its phase and frequency. The superposition of two simple sinusoidal waves serves as a suitable, if simplified, example of this process.
6. If addition is the result, then the consequence is a growing feedback loop; if subtraction is the result, the excitation is attenuated **[40]**.

In the case of energy gain, a growing acoustic field manifests with either driven or self-excited characteristics until non-linear effects intercede and introduce a finite amplitude limit cycle **[5, 7]**. The details of non-linear instability are beyond the scope of the present work, and hence any such discussion will be limited. Briefly, non-linearity as used here refers to an oscillatory system containing multiple harmonics—that is to say, multiple modes of oscillation, or in the present case, multiple acoustic modes **[18]**—such

that it is impossible to linearize the system into a summation (or linear combination) of discrete modes without information loss **[28]**. A linear system, by contrast, possesses only one harmonic, and for the case of self-excitation its growth and decay may be sufficiently modeled by an exponential function in the vein of equation **(1.1) [7, 12]**.

Regardless of linearity, acoustic instabilities induce frequency-specific pressure oscillations based on the resonant modes of the combustion chamber. Classification is first performed by frequency—low frequency, intermediate frequency, and high frequency instabilities have been designated **[11, 36, 41]**. Low frequency oscillations instabilities are observed in the approximate frequency range of 50-500 Hz, and in LREs usually arise from interactions between propellant feed systems and acoustic modes. This phenomenon, sometimes termed "chugging," is well documented, and numerous mitigation strategies exist such that these instabilities are not a serious threat **[36, 41]**. In SRMs, an additional low frequency mode—the bulk, or L* mode—is possible. This mode behaves as a classical Helmholtz resonator, and typically persists at frequencies under 150 Hz, and may even exist under 1 Hz **[42]**. This mode is not an acoustic wave mode, and hence it is not of interest to the current investigation.

Intermediate frequency instabilities (IFIs) typically span the frequency band of 500-1000 Hz **[11, 41]**. In LREs, this region of instability is termed "buzzing," and is often more a noisy phenomenon than any serious threat. Buzzing similarly is due to coupling between propellant feed system resonances, in addition to mechanical vibrations from engine operation **[42]**. Acoustic motions and the formation of entropy waves may also contribute to buzzing **[41]**. For SRMs, axial IFIs usually emerge in sufficiently long motors, and have behaviors corresponding to the classical longitudinal modes of the resonant chamber. In general, it has been assessed that IFIs usually manifest as axial modes in SRMs **[11]**.

High frequency instabilities (HFIs), typically assigned the range of frequencies above 1000 Hz, are the most commonly encountered form of instability in the development of new motors or engines. Unfortunately, energy content is directly proportional to frequency, and hence it follows that this range of instability must also be the most destructive **[42]**. In general, the term acoustic instability most often refers to this particular

class of instability, with all of the associated difficulties of prediction and mitigation. Of the instability classes, HFIs most strongly exhibit characteristics corresponding to the classical acoustic modes—discrete longitudinal and transverse modes of structure similar to that prescribed by the wave equation are observed **[36, 41, 42]**. These subclasses of instability differ in shape and severity—and more importantly, they differ in how they are damped by acoustic radiation through a nozzle. As this variance in behavior is a core component of this investigation, attention will be given to both subclasses.

It must be noted that, while ranges have been defined, and from that classes have been derived, the most important influence on the frequency and behavior of a triggered instability is ultimately the geometry of the resonating system. For example, a longitudinal oscillation that would otherwise be described as intermediate in a large scale motor may easily exceed 1000 Hz in a smaller motor—the frequency content of the excited mode is not the only criterion for classifying instabilities **[31]**.

### *2.2.1 Longitudinal Modes*

Longitudinal modes propagate on axial planes parallel to the direction of bulk flow, and hence are sometimes referred to as axial modes. They are easily visualized in a one-dimensional manner as sinusoidal waves; Figure 2.2 illustrates this. Due to the elongated configuration of a typical SRM, longitudinal modes typically occur at lower frequencies than transverse modes **[11, 43]**. This is due to the inverse proportionality of either of the significant dimensions—radius and length—with frequency that is revealed in equation **(2.24)**. In other words, a longer rocket will possess a lower frequency for a given mode of oscillation. The spatial orientation of a longitudinal mode imposes a strong relationship with the details of the attached nozzle **[11]**, such that acoustic radiation through the nozzle dominates all other damping characteristics for this mode class **[20]**. Historically, other means of instability damping that succeeded with transverse modes (e.g., the placement of baffles or the production of aluminized solid propellants) are not necessarily as effective in suppressing IFIs **[2, 11]**. This elevates the importance of nozzle damping in the suppression of axial instabilities.

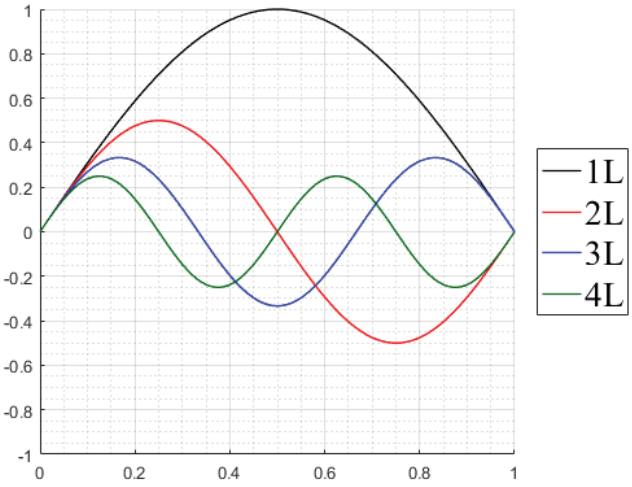


**Figure 2.2.** First Four Longitudinal Modes of Velocity of An Arbitrary, 1-D System

### *2.2.2 Transverse Modes*

Transverse modes propagate in planes perpendicular to the chamber axis and, therefore, the direction of bulk flow. This class of instability predominates in LREs, and typically coalesces in the vicinity of the injector **[42]**. Contemporary LRE design discourages the excitation of longitudinal modes by possessing smaller aspect ratios and contraction ratios. In this manner, axial modes are pushed to higher, less likely frequencies, and far more easily damped by the nozzle **[41]**. In general, transverse modes are more destructive than longitudinal modes **[36, 41, 42]**, though it is more accurate to attribute this label to the tangential subclass. That transverse modes can be reduced into tangential and radial subclasses should not be surprising, given the dual-element nature of the transverse frequency component in equation **(2.24)**

The tangential mode can be further divided into standing and spinning mode shapes. In the standing mode shape, the azimuthal positions of the node lines do not change with time **[41]**, and the mode shape behaves with alternating regions of high and low pressure

across the node line **[42]**. Figure 2.3 depicts the first few tangential and radial modes for convenience, along with three mixed tangential and radial modes. In the spinning mode shape, the amplitude remains constant—that is, the peaks and valleys remain as they establish themselves—and the entire wave rotates **[42]**. Of the transverse modes, the tangential mode has been observed to be more destructive, with heat transfer rates under the influence of this instability increasing four to ten times the stable heat transfer rate. In this manner, engine destruction through melting and wall burn-through can sometimes happen in less than one second **[41, 42]**. Referring back to Figure 2.3, an important observation can be established regarding the location of maximum amplitude. Peaks occur at locations of maximum radius—physically, this implies that the greatest pressure, and therefore greatest heat and heat transfer from combustion, would establish itself locally at the wall of a cylindrical combustion chamber. This is exceedingly detrimental, and affirms the previous statement regarding wall burn-through and engine destruction.

Further, the spinning tangential mode has been identified as possibly more detrimental than the standing counterpart due to the improved mixing of gas molecules in the transverse direction. It must be noted that this improved mixing, which increases heat-transfer rates significantly, improves the efficiency of combustion—hence, there exists a particularly troublesome tradeoff between efficiency and stability **[41]**.

There appears to be less literature focusing specifically upon the radial mode. This mode has been noted to appear only rarely in SRMs **[18]**, and is noted to be less destructive than the tangential mode, as regions of maximum pressure occur concentrically **[44]**, as can be observed in Figure 2.3. However, higher mode-number radial oscillations can produce regions of high pressure near the walls, which may improve heat transfer to the walls and adversely influence the health of the engine in question.

Baffled injectors are the most common mitigation element incorporated into a system when a transverse mode is observed—the F-1 engine being the prime example **[14, 41]**. Should the system instead be an SRM, then metallized propellants are usually sufficient in damping instabilities **[11, 18]**. In the absence of either, acoustic radiation through the nozzle remains as the only other significant loss term, though to a much

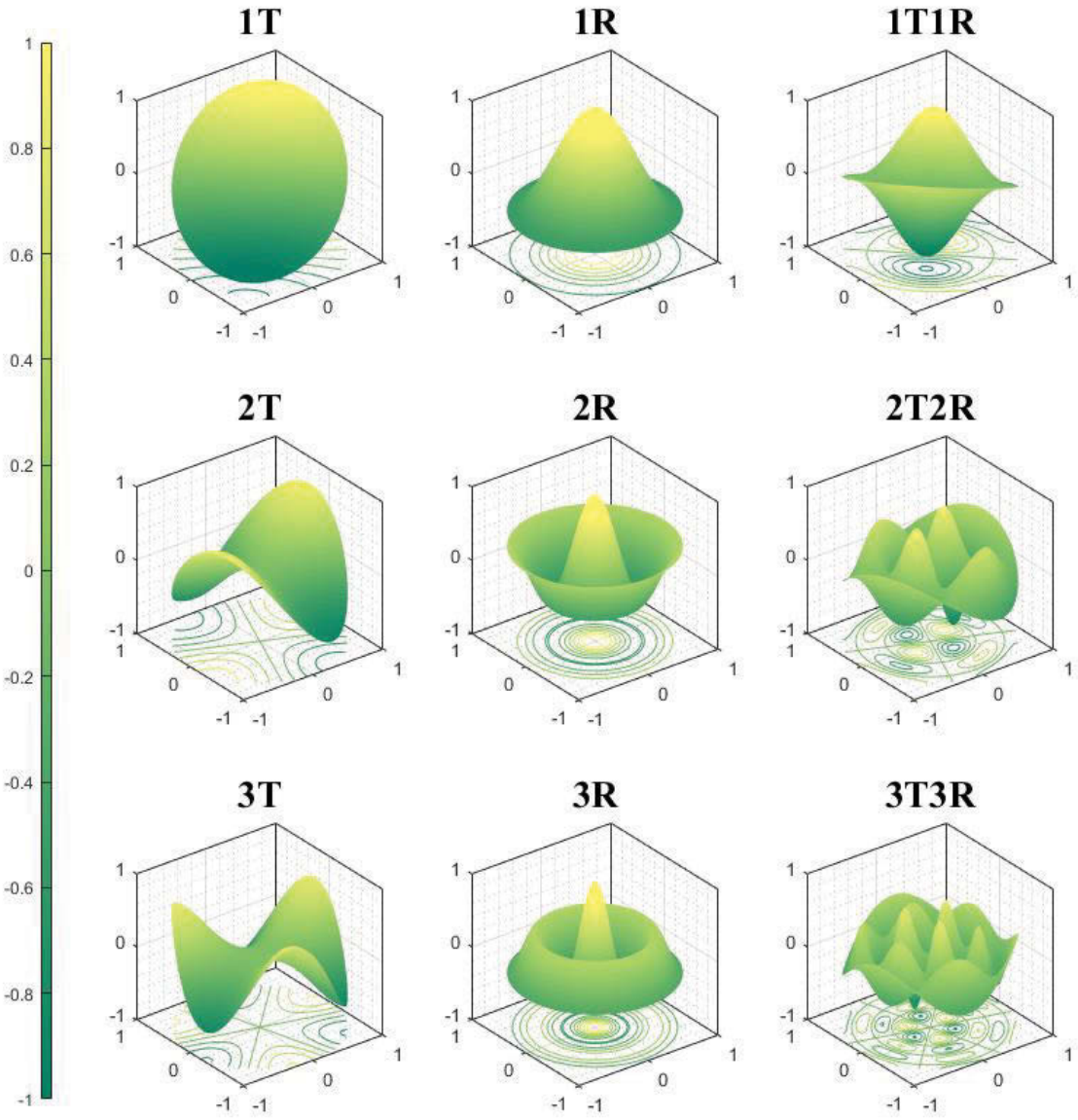


**Figure 2.3.** First Three Tangential, Radial, and Mixed Mode Shapes

reduced degree relative to the longitudinal case. To what extent this reduction exists is an important question that would appear to remain unaddressed; hence the present work seeks to address this gap, albeit in a reduced, experimental setting. This document is by no means an exhaustive theoretical study of transverse nozzle damping.

### 2.2.3 Mixed Modes and the 1T1L

Mixed modes are an oscillatory phenomena incorporating the behavior of multiple modes into a single, discrete frequency. Referring to Figure 2.3, it can be observed that the mixed modes possess both radial and tangential structures in the waveforms. Longitudinal modes can also be incorporated into mixed modes; one such mode explored in this work is known as the 1T1L mode. Visualizing the behavior of the 1T1L mode—or any mixed mode with a longitudinal component—is more difficult than for mixed transverse modes. In the case of the 1T1L, cross-sectional slices of the acoustic mode yield a 1T waveform. However, a perspective taken from the axial plane do not yield a 1L waveform. Figure 2.4 depicts an example of this view of a 1T1L mode. Owing to the 1T waveform in the cross-sectional plane, the 1T1L mode can possess the same dangers to rockets as the 1T mode with regards to the presence of higher magnitudes of pressure at the wall.

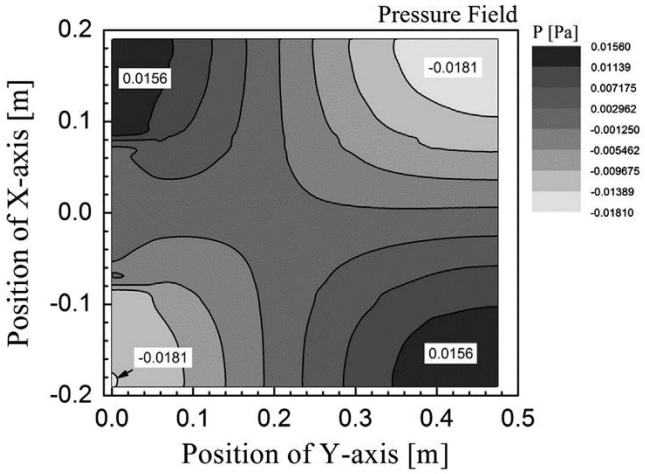


**Figure 2.4.** Side View of a 1T1L Mode **[45]**

# CHAPTER THREE
# NOZZLE DAMPING

Nozzle damping is the process by which acoustic energy is convected through the combustion chamber and out of the attached rocket nozzle, and is often times the primary impedance to the growth of instabilities. In that manner, this phenomenon has been identified as crucial to the overall stability of a rocket system, and significant resources have been expended in attempts to better understand and manipulate this process such that growing instabilities, and the issues that arise in their presence, may be avoided. What follows is a literature review presenting salient details regarding the theories and experimental methodologies that have arisen over the years in pursuit of the aforementioned understanding. Theory will be presented first such that a suitable groundwork may be present for the following discussion on known experimental methods.

## 3.1 Theory of Nozzle Damping

The theory of nozzle damping was initially established for LRE applications, and developed a parameter defined as the *nozzle admittance* **[46]**. The nozzle admittance is essential for determining the relationship between wave systems that develop within the combustion chamber and the attached nozzle. It, under certain restrictions, can be defined as the ratio of the axial velocity perturbation component to the pressure perturbation, where each term is evaluated at the nozzle entrance **[47]**. The theoretical determination of a nozzle's admittance is an involved gas dynamics problem involving a high level of mathematical complexity **[2]**, *especially* if nonlinearity is considered. As such, there exist theoretical models of a simpler nature to facilitate a more practical and less computationally expensive determination.

### *3.1.1 Fundamental Models*

The basis for most models involving oscillatory flow in a combustor and attached nozzle was derived by Crocco and Sirignano **[48]** in a report detailing the behavior of nozzles under three-dimensional, oscillatory conditions. This work served as an extension

of an earlier, frequency limited work into one valid for all frequencies **[49]**. A one dimensional mean flow assumption was imposed on the derived model, which implied a slowly convergent cross section within the nozzle, as well as an irrotational nature to the imposed oscillations **[46]**. Other simplifying assumptions were:

- The flow in the nozzle consisted only of a single, calorically perfect gas species—that is, the gas possessed constant specific heats and was unreactive.
- The flow was inviscid, and heat conduction was neglected.
- The oscillatory amplitudes of the waves were small enough such that only linear terms were necessary in the perturbation expansion **[50]**.

The key to this model rested within the application of the boundary conditions for the resulting system of differential equations. Assuming a simplified system consisting of a bare, cylindrical combustor and a conical nozzle, it follows that, for a supercritical nozzle—that is, a nozzle operating at subsonic velocity in the convergent section and at supersonic velocity in the divergent section—the throat establishes itself as a unique boundary condition. From the sonic line that establishes itself in the throat on, the velocity of the flow equals or exceeds the speed of sound, and thus permits disturbances to *only* propagate downstream. In practice, the analysis of a lumped system involving both the combustor and nozzle is cumbersome, and hence an artificial division is introduced at the nozzle *entrance*. What emerges is one system consisting only of the cylindrical combustion chamber, and the other system consisting of the nozzle entrance up to the throat. There can be no violations of continuity, momentum, etc. at this point of division, and so an artificial boundary condition defined as the *nozzle admittance* is introduced to join the two regions **[48]**. Figure 3.1 depicts this concept for a conical nozzle. The regions in blue represent areas in which acoustic propagation is considered for admittance calculations, and also where acoustic disturbances may propagate back upstream. The curved black line at the throat delineates the natural boundary condition of the sonic surface, and the bold red line illustrates the placement of the nozzle admittance which divides the cylindrical combustion chamber from the conical nozzle. The shaded red region is not used for admittance determinations, as acoustics may only travel with the flow.

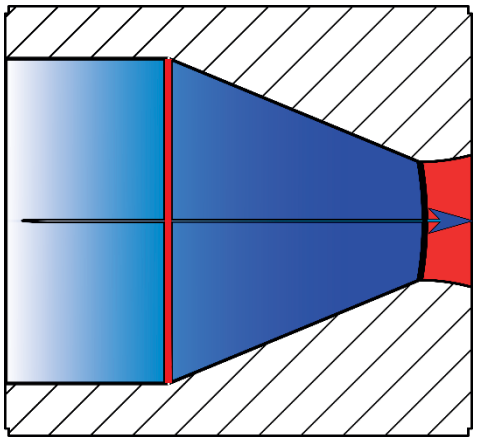

**Figure 3.1.** Boundary Conditions in a Choked Nozzle

The model derived by Crocco and Sirignano was further expanded upon by Bell and Zinn **[50]** to situations involving time-variant amplitude oscillations within the combustor and nozzle, which accounts for the growth and decay of instabilities. This study further found the one-dimensional assumption of mean flow to be valid, even in situations where the mean flow must obviously be two-dimensional **[50]**. As it relates to stability, this study presented an interesting result concerning three-dimensional oscillations, or those of the transverse class. The admittance of a nozzle is complex—that is, consisting of both real and imaginary components—quantity, and in particular the sign of the real component relates to either removal or conservation of acoustic energy. A positive real admittance implies the nozzle removes energy, and thus exerts a stabilizing influence on the system at large. A negative real admittance implies that energy is conserved, and the nozzle acts as a *destabilizing* influence on the system. Longitudinal oscillations have been observed to always possess positive real admittance values. However, this *does not* extend to the transverse modes, where negative real admittances have been observed at certain frequencies **[50]**. Zinn notes that the work performed by Crocco and Sirignano **[48]** reveals this negative admittance to be a purely three-dimensional phenomenon **[50]**.

A further simplified model was introduced by Zinn **[20, 50]** that assumed a "short nozzle." The term "short nozzle" is relative, referring to the difference between combustor

length and diameter to nozzle length and throat diameter. Zinn noted that, in most LRE instability analyses, the nozzles were assumed of sufficiently short length with small enough throat radii to classify as short nozzles **[50]**. This assumption perhaps more strongly correlates with SRMs, and as such is also of interest to this method of propulsion similarly **[20]**. The driving reduction of short nozzle theory stems from the reduced time the oscillatory waves remain in the short nozzle relative to the longer combustor. The difference in residence time permits one to assume wave reflection in the nozzle occurs instantaneously, and in this manner the problem reduces to a quasi-steady state—that is to say, quantities within the nozzle change instantaneously in the presence of perturbations imposed at the nozzle entrance **[20]**.

Applying the short nozzle assumption to the models previously discussed results in the short nozzle admittance emerging as a purely real quantity, in opposition to the complex nature it normally possesses. This implies there exists no phase difference between velocity and pressure at the nozzle entrance. In longer nozzles, this phase difference is an important quantity with significant influence on the radiation of acoustic energy through the nozzle. Furthermore, a non-dimensional nozzle admittance term for the short nozzle is observed to be small relative to the mean Mach number within the chamber, suggesting that the short nozzle behaves very closely to a solid wall boundary. In this model, most wave energy is reflected back into the combustor **[20]**. Zinn reports a discrepancy between reported data and expected results determined by the short nozzle model **[20, 50]**, suggesting that the short nozzle assumption may be difficult to justify in most cases.

Marble and Candel **[51]** further expanded upon the short nozzle model by providing a complete, one-dimensional, non-steady treatment of the acoustic disturbance generated by the passage through a nozzle by an unsteady gas. Their work, as applied to disturbances of wavelength much greater than nozzle length, was based on the observation that said nozzle appears less as a geometrical boundary and more as a discontinuity in the propagating medium, in a manner similar to a standing shockwave **[51]**. What emerged was an analytical relationship coupling the Mach number within the chamber and nozzle

to the incident and reflected pressure waves. Hence, short nozzle stability could be estimated through knowledge of the operating Mach number **[49]**.

Figure 3.2 depicts Zinn's original schematic involving wave propagation in a convergent nozzle. With the exception of the element at the throat, each slice has oscillatory pressure terms propagating upstream and downstream. In addition to the changes in properties brought about by the convergence of the nozzle under steady conditions (i.e., temperature, density, pressure, Mach number), these properties are similarly influenced by the unsteady pressure terms. The complexities associated with nozzle damping are made more obvious when one observes that a change to either a steady state variable, or the rate of change of the unsteady component, influences all other variables, to say nothing of the boundary conditions which contain the variables.

### *3.1.2 Driving Mechanisms*

The wave motion inside the nozzle, consisting of both incident and reflected pressure waves, is the determining factor of nozzle damping **[37]**. Referring back to the short nozzle model, a high degree of reflection was observed, and correspondingly the damping effect of the nozzle was small **[20]**. This similarly extends to nozzles of appreciable length; a high amount of reflection in the nozzle corresponds to the system

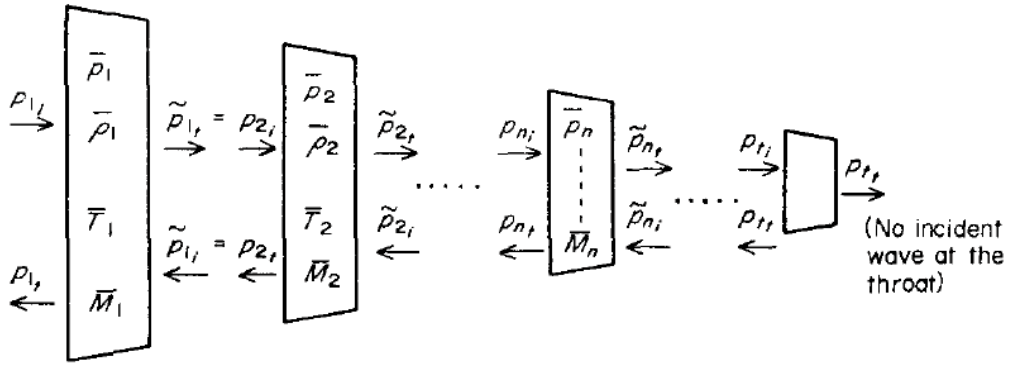


**Figure 3.2.** Zinn's Schematic of Wave Propagation Through a Nozzle **[20]**

being energy retentive. Disregarding the influence of combustion and other potential damping mechanisms (e.g., metal particles in the medium), the problem of acoustic propagation is heavily influenced by the imposed boundary conditions. As an extreme example, the propagation of acoustic waves through a constant diameter pipe is of a different character than the propagation of waves through a convergent duct. The driver of this difference lies with the reflection that must occur when sound strikes a surface. In the case of purely one-dimensional wave transmission, the straight pipe imposes no such surface upon which waves might reflect, whereas the converging duct obviously imposes an obstructing surface area that must reflect waves.

The characteristics of the reflected wave depend strongly upon the characteristics of the reflecting surface, and the adjoining surfaces **[25]**. For the purposes of this investigation, all surfaces will be assumed impenetrable to acoustic radiation, and the surfaces will be entirely stationary with no vibratory motion. In this manner, reflection reduces to a geometrical problem concerning the normal vector of the incident surface, and the angle of incidence for the incident wave **[25]**. Recalling that waves cannot propagate upstream beyond the throat, and assuming a simple cylindrical combustion chamber—the length and radius of which contributes primarily to the resonant frequencies of the system—then the only remaining influential geometry must be the convergent section of the nozzle. Indeed, the acoustic losses for a rocket nozzle of a given contraction ratio depend upon the geometry of contraction **[1]**. Insofar as longitudinal modes are concerned, a conically convergent section has been found to provide more damping than other tested geometries. A larger phase shift between incident and reflected waves at the nozzle entrance was observed, which would appear to indicate that the conical nozzle appears "longer" to the incident oscillations **[1, 2]**.

Another important mechanism that would be prudent to briefly address is the manner in which the combustor and nozzle are attached. By that, it is meant if the nozzle attaches directly to the combustor, or if the nozzle is "submerged." In a submerged configuration, the nozzle is recessed within the combustion chamber some distance. Admittance behavior is strongly dependent on the cavity depth that surrounds the nozzle

**[1]**. The present work does not involve submerged nozzles, and hence the subject will not be discussed further—however, it is yet another extremely important consideration that must be remembered when designing for stability.

### *3.1.3 Admittance and the Decay Rate*

Zinn **[20]** noted that an inconsistency existed in reported nozzle damping data—in some instances, the admittance would be reported, and in others, something known as the nozzle decay rate would be reported. In the interest of parity, partial theory of both will be briefly outlined. Recall that admittance is defined as the ratio of the velocity perturbations to the pressure perturbations at the nozzle entrance plane. Equations **(3.1)** and **(3.2)** present, respectively, the velocity and pressure perturbations as derived by Zinn **[20, 22]**; *Re* denotes the real component of a complex number, the subscript *N* designates a quantity measured in the nozzle, the subscript *p* designates a perturbation quantity, *P* represents pressure, *U* represents velocity, $\omega$ is the angular frequency of oscillation, and $\theta$ is the phase difference between velocity and pressure perturbations.

$$U_p = Re(|U_N|e^{i(\omega t+\theta)}) \tag{3.1}$$

$$P_p = Re(|P_N|e^{i\omega t}) \tag{3.2}$$

The nozzle admittance, *Y*, may then be expressed as **[20, 22]**:

$$Y = \frac{U_p}{P_p} = \frac{|U_N|}{|P_N|}e^{i\theta} \tag{3.3}$$

In the case of zero phase difference, the admittance reduces to a purely real term—recall that this is the behavior observed in short nozzles. Otherwise, the admittance is a complex quantity, and the sign thereof is determined entirely by the imposed phase difference. Note that the real component of the admittance reduces to the following:

$$Re(Y) = \frac{|U_N|\cos(\theta)}{|P_N|} \tag{3.4}$$

Thus, for values of $\theta$ between $\pi/2$ and $3\pi/2$, the real admittance is negative, and the system is energy retentive.

How the phase difference arises is a matter of acoustics. Specifically, the phase difference emerges as a result of the reflection of pressure waves within a cavity. These reflected waves may sum with the incident waves travelling against them, and by superposition the two coalesce into a resonant, standing wave. Suppose resonance emerges in an open-closed pipe—a configuration like an organ pipe, or approximated by a subcritical combustor-nozzle combination. The standing pressure wave establishes an antinode, or point of maximum amplitude, at the closed end. A node, or point of zero amplitude, is established at the open end. To be physical, the velocity wave must establish a node at the closed end, as it cannot penetrate the wall—recall that the velocity wave pertains to particle displacement, and non-zero velocity at the wall is physically impossible for an impenetrable boundary. In this manner, pressure and velocity are immediately made $\pi/2$ radians out of phase **[25, 26]**. It must be noted that this assumes undamped, perfect resonant behavior. The influence of damping, which all real systems must possess to some degree, introduces a slight frequency shift **[25]**. Further, due to the influence of the convergent section, and the open end observed in a rocket configuration, it is not entirely accurate to state that a purely standing wave emerges, and that pressure and velocity are exactly $\pi/2$ radians apart; the difference that does emerge is tied to the geometry and physical conditions of a particular setup. Through this the geometry of the convergent section of a rocket nozzle can considerably influence the long-term stability of a rocket system.

Another method of reporting nozzle damping statistics is by means of a nozzle decay rate. Determining the theoretical decay that may be attributed to the nozzle requires an assumption that nozzle damping is the only loss mechanism present, which in many circumstances may be a poor assumption **[33]**. The admittance of a nozzle can be coupled into the equations for the nozzle decay coefficient such that knowing the admittance can lead to a determination of the decay rate, which is typically denoted as $\alpha$ **[20]**. Short nozzle theory can be applied if the decay of the nozzle is anticipated to be low, as would be in the case of a poorly admitting nozzle, and the decay reduces to a simple relationship tied to the mean Mach number **[20]**:

$$\alpha_N \simeq -\frac{\left[\bar{M}\bar{a}\left(\frac{\gamma+1}{2}\right)\left(1+\frac{\gamma+1}{2}\bar{M}^2\right)\right]}{L_c} \quad \textbf{(3.5)}$$

Here, symbols with an overbar are mean quantities; $L_c$ is the length of the combustor; and $\gamma$ is the ratio of specific heats.

## 3.2 Experimental Methods

The complexities associated with the numerical determination of nozzle admittance and decay have provided significant incentive towards the experimental determination thereof. In this manner, several experimental techniques have arisen over the years. A few key examples, with their applications, merits, and detractors, will be discussed.

### *3.2.1 Direct Technique*

The *direct technique* was originally developed by Crocco, Monti, and Grey **[52]**, who determined the complex nozzle admittance from direct pressure and velocity measurements at the nozzle entrance plane **[37]**. This was facilitated by the installation of a hotwire anemometer probe and pressure transducer installed at the entrance plane. There exist numerous experimental difficulties with this method, and the inaccuracies associated with the measurement of velocity perturbations further degrade recorded results for admittance **[2, 22]**.

### *3.2.2 Wave Attenuation Technique*

The wave attenuation technique, known also as the decay technique, analyzes the resonant decay of a pressure pulse imposed within a chamber operating with mean flow. The measured decay rate is used to determine the nozzle admittance **[2]**, though it could also produce a nozzle decay rate **[53]**. This technique has experimental difficulties when damping is large due to the extremely fast decay of the resonant wave. Further, this method implicitly assumes that nozzle damping is the sole damping mechanism present **[2]**. Evidence exists that, depending upon the mode shape, viscous losses may be significant **[33]**, and hence the assumption that nozzle losses are the sole losses is open to question. The measured admittance or decay coefficient determined from this method is applicable

only to the imposed frequency; investigations interested in multiple modes (e.g., 1L, 1T1L, 1T, etc.) must have a mechanism in place to alter that chamber such that the desired mode is the frequency formed by the pressure pulse. This is a serious limitation to an otherwise extremely attractive method, especially when nozzle response over a wide frequency range is of interest **[2, 22, 54]**.

### *3.2.3 Frequency Response Technique*

The frequency response, or steady state resonance technique, involves the generation of pressure waves of different frequencies within a chamber. **[22, 54]** The oscillatory amplitudes of each frequency are then measured. At the resonant frequency, power transferred from a given driver system is maximized, and away from this frequency the power accordingly drops; the acoustic response of the chamber thereof with respect to the frequency forms a resonance curve that can be used to determine the nozzle admittance **[21]**. Analyses performed on this method suggests it is only applicable to nozzles with admittances independent of frequency **[2]**, which is a severe detraction.

### *3.2.4 Modified Impedance Tube Technique*

The modified impedance tube method, as its name may suggest, is an extension of the classical, no flow, impedance tube method of classical acoustics **[2]**. In the classical method, a sample of unknown acoustic impedance is placed at the closed end of an open-closed tube, and acoustic radiation is imposed through the system. The incident wave experiences a quantifiable change in amplitude and phase upon reflection from the sample. Reinforcement and interference facilitated by superposition of the incident and reflected waves enforces a standing wave arrangement with fixed maxima and minima; the ratios and locations thereof are used to determine the impedance of the sample **[25, 55]**. Measurement is facilitated by a microphone probe that is permitted to traverse the axial plane of the system, and thus map out the pressure distribution in the tube. Further, the classic technique permits the simple acquisition of frequency dependent data, as all that is necessary is to change the frequency imposed on the tube—in other words, only the characteristics of the driver need be changed **[2]**.

In the modified impedance tube technique, a driver capable of producing acoustic waves at specifiable frequencies is attached to a simulated rocket chamber; the other end of the chamber is attached to the nozzle, which can be viewed as an analogue to the sample material in the classical method, with the caveat being that *admittance*, rather than *impedance* is the desired quantity. As with the classical method, the modified technique relies upon measurements of the amplitudes and phases of resonant standing waves **[1]**. Discrete pressure transducer or microphone locations, rather than a single traversing instrument, have appeared to emerge as a preference when dealing with the inclusion of mean flow and compressibility induced by a convergent nozzle **[2]**. This method is similarly not limited to the resonant frequencies of the attached combustor and nozzle, and hence suffers none of the serious detractions observed in other methods **[54]**. Culick and Dehority **[13]**, in an investigation of the applicability of the experimental methods available for quantifying nozzle admittances, reached the conclusion that the modified impedance tube method appeared to be the most suitable technique available. Bell **[47]**, independent of Culick and Dehority, reached a similar conclusion **[1, 2, 22]**.

It must be noted that this technique requires a *minimum* of three discrete points of measurement—that is, three pressure measurements at three axially unique locations—to determine three unknown variables. However, possessing only three discrete points of measurement introduces severe variability in the recorded admittance, and hence no reliability is possible with the minimum. Physically, it is understood that three points are not able to accurately characterize the perturbed standing wave pattern that is established in the combustor—rather, a number of discrete points of measurement exceeding three is necessary for reliable data **[47]**. As with a finite element analysis, a greater number of discrete points will yield more accurate data.

## 3.3 Previous Nozzle Damping Studies

A number of studies devoted to nozzle damping of both experimental and numerical natures have arisen over the years **[1-3, 10, 37, 38, 47, 49, 50, 53, 54, 56, 57]**, and much information can be gleaned from analyzing both methods and results. Of most interest to

the current work are those investigations involving purely acoustical effects, and those involving different convergent test sections. From these, the basis of the present investigation is established, from anticipated results of known configurations, to the methods of evaluation. The most relevant of such studies, as they relate to this investigation, will be outlined in the following sections.

### *3.3.1 Foundational Investigations*

The foundation of experimentation as applied to acoustic losses in a rocket system was established in 1968 by Culick and Dehority **[13]**. In a report dealing with the analysis of acoustic waves in a purely cold-flow experiment, the most significant fundament for all future investigations was observed: the strong dependence of losses on geometry, and the necessity of an attached combustor, scaled or otherwise **[13]**. This particular observation can be viewed as a guiding principle for experimental studies involving nozzle damping.

As it relates the present work, the analyses performed by Bell and Zinn **[37, 47, 50]**, and Janardan and Zinn **[1, 2, 54]** on the experimental determination of admittance and damping characteristics of rocket nozzles is of particular interest. As previously mentioned, Bell's work served as an independent validation of the modified impedance tube method for both axial and mixed first tangential-longitudinal modes. However, to reach this point, it was necessary to expand the classical impedance tube technique—itself a strictly one-dimensional, no flow analysis—to permit the existence of three-dimensional oscillations and mean flow. The results obtained from this modified method with regards to longitudinal modes agreed with values from the theory developed by Crocco. For the mixed 1T1L mode, the imaginary values similarly aligned; however, the real component of the admittance differed by a minus sign. It was determined that phase measurements, which Bell was unable to employ due to experimental limitations, are necessary for determining the sign of the real component **[47]**. Recall that the sign signifies whether the nozzle is a stabilizing or destabilizing influence on the system.

The work performed by Janardan and Zinn with regards to the damping characteristics of three convergent nozzle contours serves as the primary foundation of the

present work. While this study focused upon the damping of three similar contours, Janardan's was far larger in scope. Briefly, the analyses so performed included investigations into submerged nozzles, the geometry of the convergent section of nozzles, and the number of nozzles present in a multiple nozzle cluster. Further, the necessary criteria for scaling cold-flow, small-scale admittance test data to actual engine parameters were determined **[2]**. As with Bell, admittance data were collected via the modified impedance tube method. Both pressure amplitude and phase data were recorded in this investigation to facilitate the admittance calculations. As previously mentioned, the tested nozzle sections were conical, ER, and LVP in convergence. For reference, Figure 3.3 depicts the three tested configurations. For low frequency axial oscillations, the three configurations were observed to possess approximately similar damping rates. Only at higher frequencies do dissimilarities emerge, with the conical nozzle dominating the others in axial damping **[1, 2]**.

### *3.3.2 Transverse Mode Damping*

Recently, research into 1T mode damping has emerged from the Technische Universität München. The experimentation was to validate numerical models of this particular instability mode **[3, 38, 57]** and the experimental methods are of interest to the present investigation. This experiment required excitation at various *eigenfrequencies*—otherwise known as resonant frequencies—which in turn required a frequency-tunable excitation system. A pneumatic siren provided the necessary acoustic forcing. Frequency variance was enabled through control over the rotation speed of the siren disc, which possessed slots through which air was driven at constant pressure and mass flow rate **[38]**. Two discs were available for testing: one with a sequence of nine slots separated by 6.4 degrees, and one with 56 slots of the same spacing around the entire circumference **[57]**. Figure 3.4 depicts both siren discs, as well as an interior schematic of the siren. The different discs permit different avenues of stability testing. The pause in pulsing that resulted from the solid portion of the nine-slot siren provided a time for the attenuation of

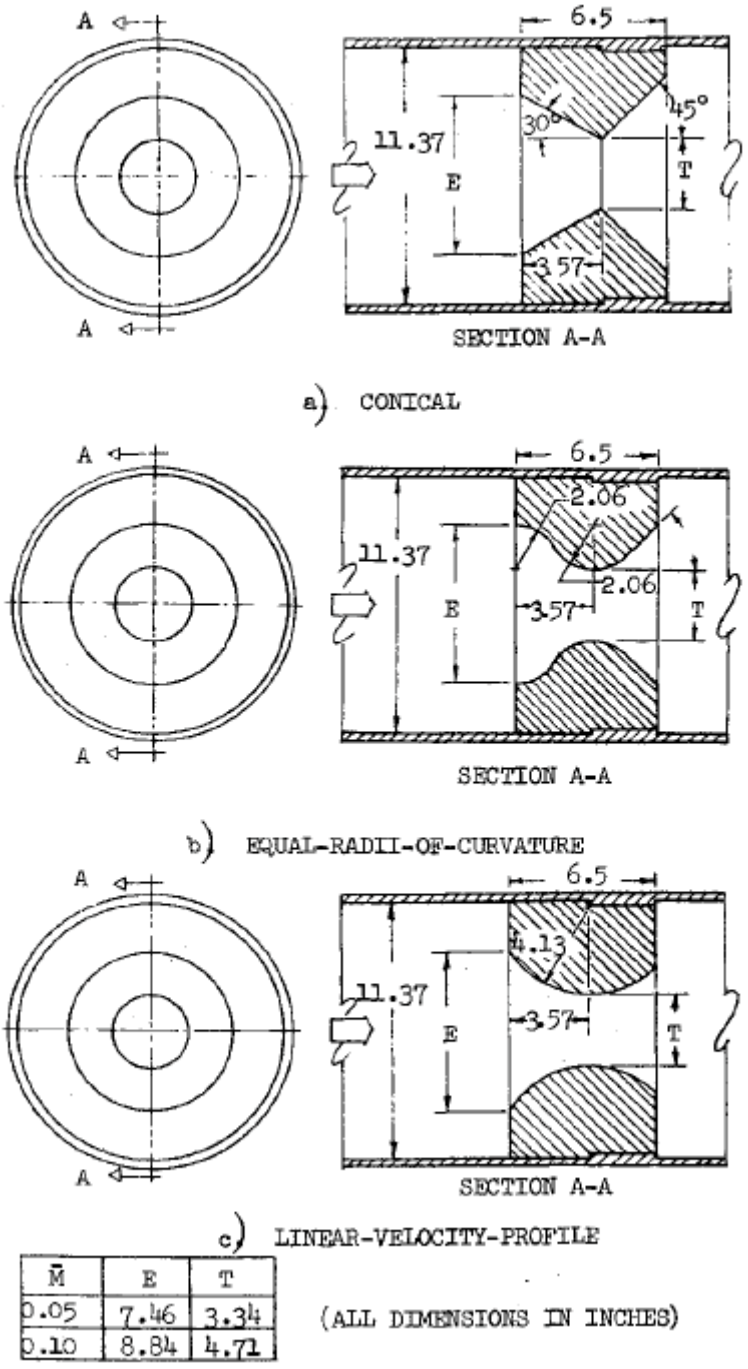


| $\bar{M}$ | E | T |
|---|---|---|
| 0.05 | 7.46 | 3.34 |
| 0.10 | 8.84 | 4.71 |

(ALL DIMENSIONS IN INCHES)

**Figure 3.3.** Janardan's Conical, ER, and LVP Nozzles **[1]**

the acoustic signal, before being pulsed again. In this manner, several growth and decay measurements were facilitated. Admittance studies were facilitated by the other disc, which permitted constant pulsing. Further, this disc was also employed in determining eigenfrequencies **[57]**.

Five different experimental methods in total were used to characterize the damping of the 1T mode, and to provide a sufficient quantity of data for the validation of numerical models. Briefly, these methods were:

- Continuous excitation by system noise primarily driven by inflow and outflow through a perforated plate at the chamber entrance. Pulsing frequency and decay rate were determined from a resonance curve over which a Cauchy-Lorentz distribution was applied.
- Periodic harmonic excitation by the nine-slot siren disc. Damping was determined by analysis of the envelope of the pressure signals following a Hilbert transformation.

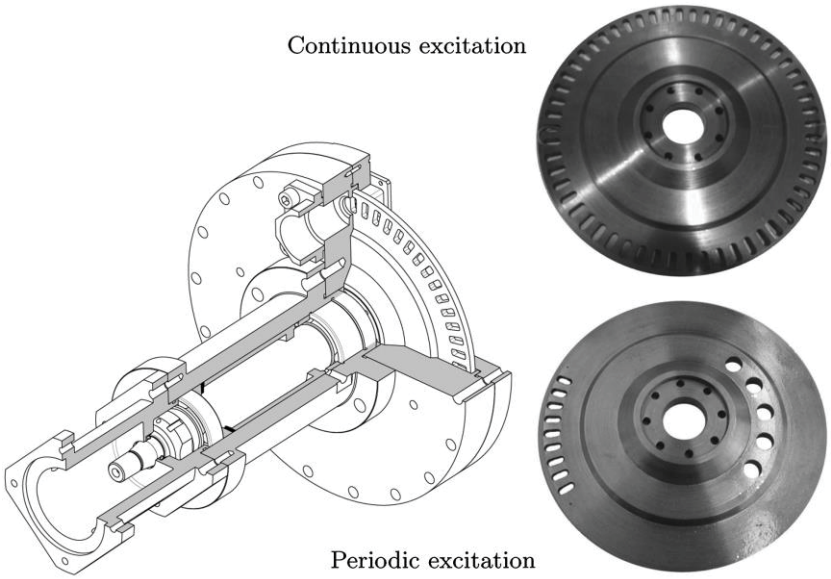


**Figure 3.4.** Pneumatic Siren and Rotary Discs **[57]**

- Periodic harmonic excitation by the nine-slot siren disc. Damping this time was determined from the Fourier transform of the attenuating pressure signals.
- Continuous harmonic excitation by the 56 slot siren disc. Pulsing frequency and decay rate were again determined from a resonance curve.
- Periodic harmonic excitation by the nine-slot siren disc. Damping data is derived from the measured acoustic decay **[57]**.

The fifth experimental method was chosen as the method that provided the most accurate damping data. Interestingly, the results collected demonstrated the dominance of the perforated plate, which acts as a flow straightener, on the overall damping processes within the test article. An $\alpha$ of approximately -573 inverse seconds was recorded with the fifth evaluation method for a system including the perforated plate. Using the same evaluation method to determine just the nozzle decay rate produced an $\alpha$ of only -63 inverse seconds. Note that both studies only analyzed the 1T mode **[56, 57]**. Physically, the damping provided by the perforated plate results from the interaction between a downstream shear layer and the acoustic properties of the plate, which lead to the production of vortical structures **[58]**.

This investigation determined that damping resulting from the perforated plate cannot be avoided due to the high velocities that result regardless of plate porosity. Consequently, measured damping statistics are usually much higher in these models than in real rocket engines. Further, it was observed that this makes it difficult to accurately extract the nozzle's contribution to decay. Despite this, however, when supplied with the experimentally determined admittances, the applied numerical models tended towards replicating the experimental results **[57]**.

As it pertains to the present work, the experiments performed by Kathan et al. **[3, 38, 56-58]** serve to validate the use of an acoustic siren for the purposes of exciting at least the 1T within a test geometry. Further, the experiments performed with the nine-slot siren disc serve as proof that damping estimates facilitated by acoustic attenuation measurements are indeed possible when pulsing with a siren.

# CHAPTER FOUR
# EXPERIMENTAL DETAILS

A set of six pressure transducers were available for use in this experiment, and provided the means of measuring the pressure data necessary to determine the nozzle admittance and decay of the three test sections. To induce the necessary acoustic modes, a frequency-tunable siren fed with compressed air of pressure controlled by an attached regulator was used. The siren disc used for all test runs possessed slots around the entire circumference, thus providing constant acoustic excitation while in operation. To permit the study of acoustic decay, a fast-action spring-activated gate valve was installed between the siren and test geometry, and upon activation removes the influence of the excitation provided by the siren. Details of the aforementioned components are provided in the ensuing sections, followed by a description of the test procedures used to acquire data.

## 4.1 Experimental Arrangement

### *4.1.1 Air Supply System*

All nozzles were designed to have a choking pressure of approximately 1.89 times atmospheric pressure, or nominally 28 psia at sea level. A sufficient, compressed air supply was available at the university; however, circumstances were such that it was not possible to perform the proposed mean flow tests. The air supply for the pneumatic siren originated from a separate system—an air compressor with a nominal operating pressure of 150 psig. The pressure into the siren could be measured and controlled by a regulator installed between the delivery line and siren housing, but for most test runs the regulator was fully open at 100 psig.

### *4.1.2 Pneumatic Siren*

The rotor of the siren was designed similar to the circumferentially slotted disc used by Sattelmayer, et al. **[57]** such that the only mode of operation was constant excitation. To induce the necessary rotation, a WATTSAVER C145T34FB33C 2 horsepower AC

motor was connected to the siren housing via a mechanical belt. An ESV152N04TXB Lenze AC Tech SMVector frequency inverter permits a variable voltage input to the motor, and thus allows for frequency control over the siren.

A critical consideration for all tests involving the pneumatic siren was the quality, or pureness, of the tone used to excite the 1T mode. An experimental test involving the siren exhausting into open air was carried out, with one of the six available transducers positioned near the exhaust port of the siren. The rotary disc was supplied the necessary voltages to perform a set of frequency sweeps over the range from 500 to 3500 Hz; Figure 4.1 depicts a cumulative plot of many windowed fast-Fourier-transforms (FFTs) applied to the data collected by the transducer for various excitation ranges between 500 and 3500 Hz. Figure 4.1 reveals the siren has poor acoustic purity below 1000 Hz, and above 3000 Hz. At low frequencies, several harmonics of equal strength to the fundamental driven frequency can be identified; Figure 4.1a) presents the clearest picture of this. These harmonics are extremely detrimental to the testing described in this manuscript, and this was one of several issues that forced low-frequency, longitudinal mode studies to be abandoned. At higher frequencies, the siren fails to provide a discrete frequency, and tends towards the production of white-noise. For this reason, higher frequency mode analysis—as likely required of any radial modes—was similarly abandoned. The siren provided acceptable purity and strength from about 1500 Hz to 2000 Hz, such that any frequencies within this range could be reliably driven without contamination.

### *4.1.3 Test Nozzles*

In an attempt to avoid the expenses associated with fiberglass or aluminum nozzles, a decision was made to construct them from a pourable, mineral-filled urethane casting resin **[59]**. This particular material was used successfully in a previous experiment with a much larger rocket nozzle, and hence there did exist a degree of familiarity with the material and casting process. To facilitate the use of the casting resin, it was first necessary to construct the interior molds around which the resin would be poured. The molds were designed in SOLIDWORKS, and printed by a Makerbot Replicator 2X using acrylonitrile

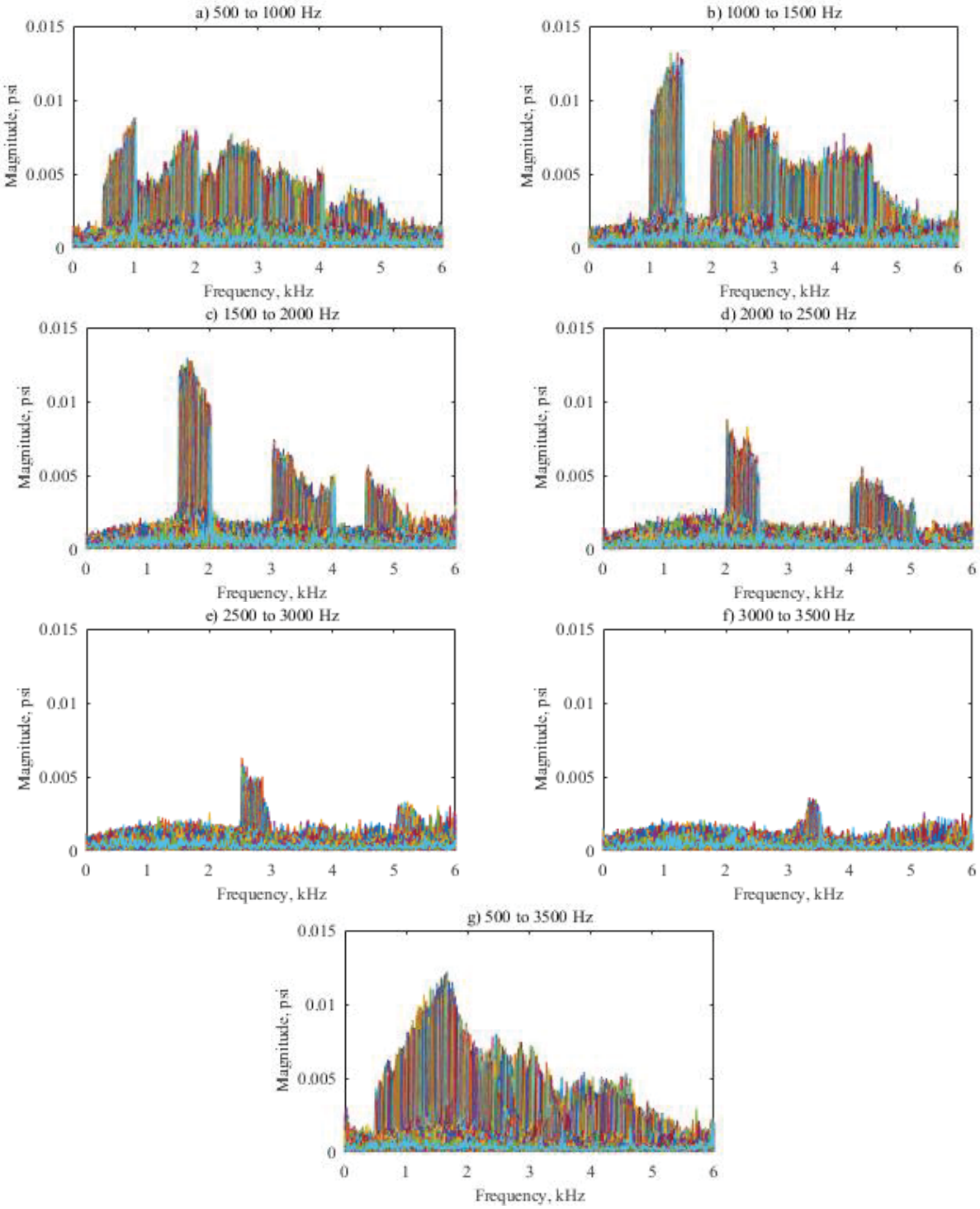


**Figure 4.1.** Frequency Response of the Siren Exhausting to Ambient Conditions for Various Excitations Between 500 and 3500 Hz.

butadiene styrene (ABS) plastic. There were a number of difficulties associated in the three-dimensional printing process—the most prevalent being a curling at the base of the material on prints with excessive manufacture times. Despite such impedances, satisfactory molds were eventually printed. The molds were placed within a 7.25 inch inner diameter acrylic tube, and a centering ring that fit the inner diameter of the tube and outer diameter of the mold base ensured that, once poured, the hollow section of the nozzle was approximately centered. Following the pouring process, and the ensuing curing period, the nozzles were initially post-processed by hand. This involved sanding down any rough spots and filling in voids such that the interior of the nozzle was made relatively smooth. Finally, the nozzles were then machined to specification, which included the drilling and tapping of transducer ports.

The design of the converging sections was derived from Janardan's **[2]** axial experiments. In the portion of his investigation involving the convergent section of a nozzle, he examined three geometries: a conical geometry, an ER geometry, and an LVP geometry. Three similar geometries are examined in this investigation. Figure 4.2 details the nozzles as they were initially designed. Upon inspection, it should be apparent that the nozzles only differ by the manner in which the equal length convergent sections converge. All other dimensions (e.g., throat radius, combustor length, etc.) are equal. Supposing that the nozzles are fed exactly the same upstream conditions, observed differences in flow effects and acoustic properties would be due to the differences in convergence.

In order to facilitate the pressure measurements necessary to determine acoustic characteristics, a number of transducer ports were drilled and tapped into each nozzle. A row of six such ports were placed at the zero degree point of each nozzle for longitudinal measurements and admittance determination. Similarly, five other ports were placed in a clockwise fashion at 70, 90, 115, 270, and 310 degrees for the transverse modes. This placement was chosen due to the lack of coincidence (with the exception of the 90 and 270 degree ports) such that node lines could not easily align and thus preclude useful pressure measurement. Further, two additional holes were placed at the 270 degree mark to accommodate $3/8^{th}$ inch NPT fittings, which both the siren air delivery system and a

common-pressure manifold for the transducers require. Figure 4.3 depicts the tangential ports locations common to all three chambers, and Figure 4.4 illustrates the locations of the longitudinal ports relative to the nozzle entrance. Table 4.1 provides a reference for these locations. Note that, while the conical nozzle is depicted in this figure, all nozzles were designed to possess the same port locations.

### *4.1.4 Instrumentation and Data Acquisition*

The six transducers were all Meggitt Endevco® 8510B-2 piezoresistive pressure transducers. This particular model possessed a 0-2 psi range sensitivity, which was necessitated by the magnitude of output pressure from the siren. Referring back to Figure 4.1, it can be seen that the maximum output is approximately 0.0125 psig, even with minimal acoustic dispersion facilitated by having the transducer at the exhaust port. While this figure can be considered as a benchmark for off-resonant frequencies within the test geometries, it cannot be considered a typical figure for resonant frequencies, which are expectedly larger.

Data acquisition was facilitated by an NI cDAQ 9184. All data were sampled at 40 kHz to safely avoid any aliasing concerns. Control over the experiment was provided by a LabVIEW virtual instrument (VI). In this VI, a voltage command from 0-10 V could be supplied to the motor, which in turn controlled the frequency output of the siren. The relationship between voltage and frequency was approximately linear such that the slope could be defined as 450 Hz per 1 V. The effective resolution extended down to $10^{-2}$ V, such that a measureable difference in frequency could be discerned between 3.14 and 3.15 V. Ideally, the frequency output of the siren would be constant; however, in practice it was quickly observed that a drift on the order of ±5 Hz was present at every set point. This drift is visible in all collected data, but does little more than induce a difficult-to-filter oscillatory pattern to frequency-specific waveforms extracted from the raw signals.

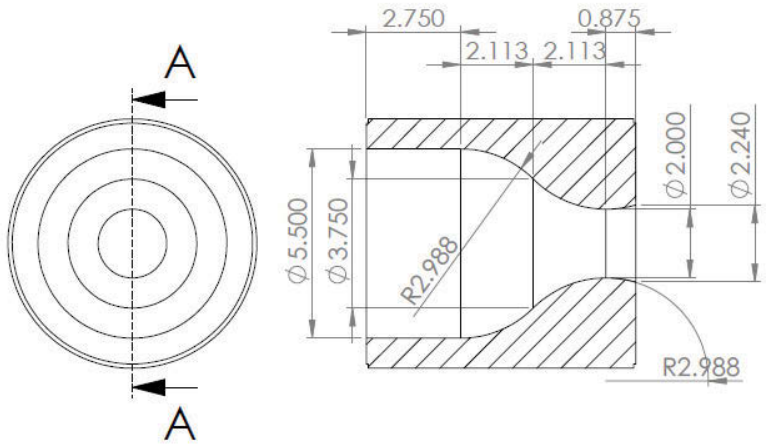


a) Equal-radius-of-curvature

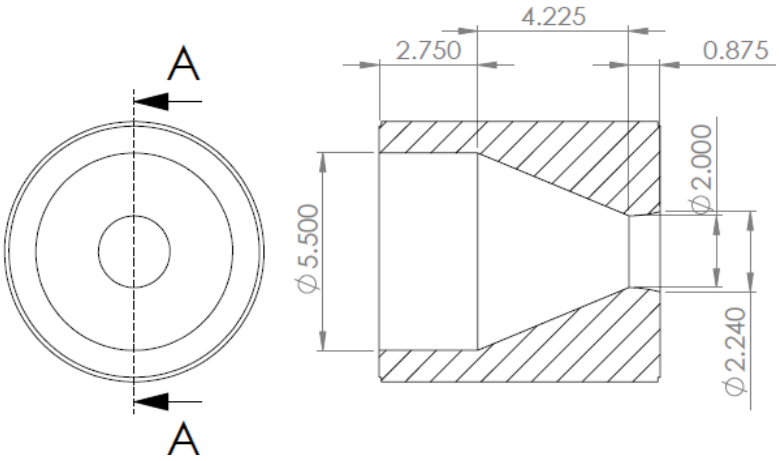


b) Conical

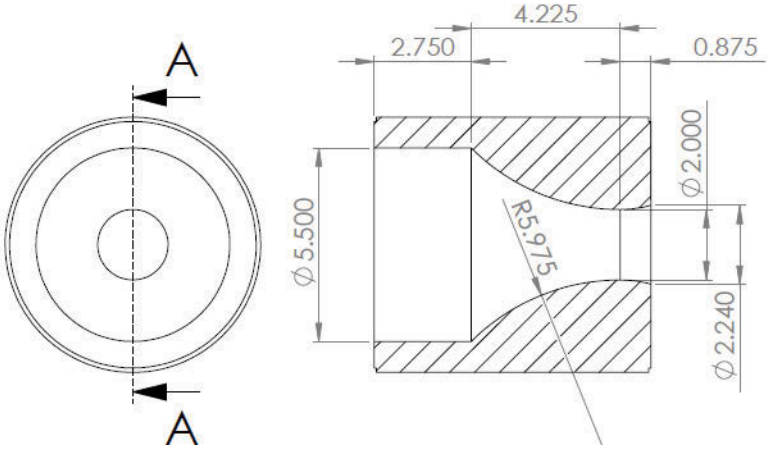


c) Linear-velocity-profile

**Figure 4.2.** Nozzle Schematics. All units in inches.

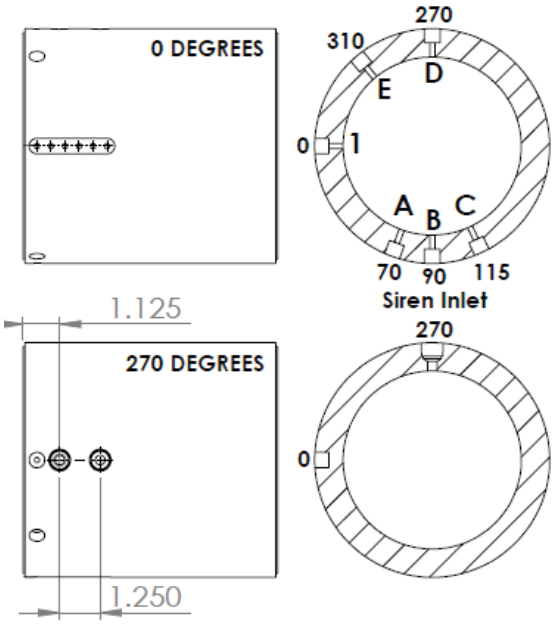


**Figure 4.3.** Tangential Transducer Port Locations and the Siren Inlet. All Units in Inches

**Table 4.1. Transducer Locations**

| Port Label | Tangential Position (degrees) | Longitudinal Position (inches) |
|---|---|---|
| 1 | 0 | 0.425 |
| 2 | 0 | 0.8575 |
| 3 | 0 | 1.29 |
| 4 | 0 | 1.7225 |
| 5 | 0 | 2.155 |
| 6 | 0 | 2.5875 |
| A | 70 | 0.425 |
| B | 90 | 0.425 |
| C | 115 | 0.425 |
| D | 270 | 0.425 |
| E | 310 | 0.425 |

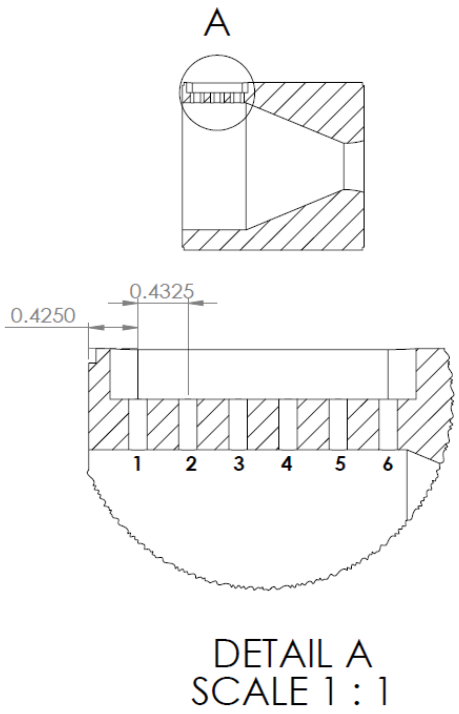


**Figure 4.4.** Longitudinal Transducer Port Locations. All Units in Inches

### *4.1.5 Gate-Valve*

Since the rotor used in the siren permitted only constant excitation, it was necessary to pursue a means of shutting off the oscillatory flow into the nozzle in order to measure acoustic decay. Two critical criteria existed for this mechanism:

- The mechanism must be able to act on the order of a few milliseconds. Slower activation times would lead to contaminated decay rates, as the siren would still be introducing oscillatory flow into the nozzle until fully stopped.
- The mechanism must be able to be placed at, or extremely close to, the test-geometry siren-inlet. This is a two-part concern:
- Any length of tubing between the mechanism and the test geometries would possess their own acoustic properties—shorter tubes would have fundamental modes high

enough to avoid introducing an acoustic mode from the delivery tube into the nozzle.

- Longer tubing length would incur longer residence times for the remaining air between the mechanism and test article. The faster the delivery tube exhausts all oscillatory flow into the nozzle, the more pure the acoustic decay result that emerges from the nozzle.

Other criteria, such as simplicity and cost, were similarly considered. To that end, it was decided that an in-house, 3D-printed, spring-activated gate-valve would be sufficient for the purposes of this experiment. Figure 4.5 depicts three views of the final design of the gate-valve. The design as depicted accommodated the use of a photogate for timing the closing of the gate-valve. While the use of the photogate was later rejected due to several issues, the device permitted the determination of the activation time of the valve. This activation time from fully open to fully closed was on the order of four milliseconds, which sufficiently meets a requisite criterion. Provided there is no photogate installation present, this valve is also able to be placed within an inch of the test-geometries, thus satisfying the second critical criterion.

The valve was printed from ABS plastic in the same printer used for the nozzle molds. A 10 lbf (44.5 N) spring was used to force shut the valve upon removal of the stopper rod, which occupied the bottom hole of the plunger. The spring's compression could be varied by means of a threaded rod passing through a bolt attached to the top of the valve. Upon full closure, the top hole of the plunger would rest where the bottom hole had previously been, allowing a laser (when the photogate was in use) to pass through. Similarly, the stopper rod was used to reset the valve to the original, fully open position by lifting up once through this top hole. In this manner, the use of the valve was a simple, repeatable process that, theoretically, introduced little contamination to the data.

One significant drawback to the use of this gate-valve, however, emerged in the form of unforeseen pressure loss. When fully open, a significant amount of air was

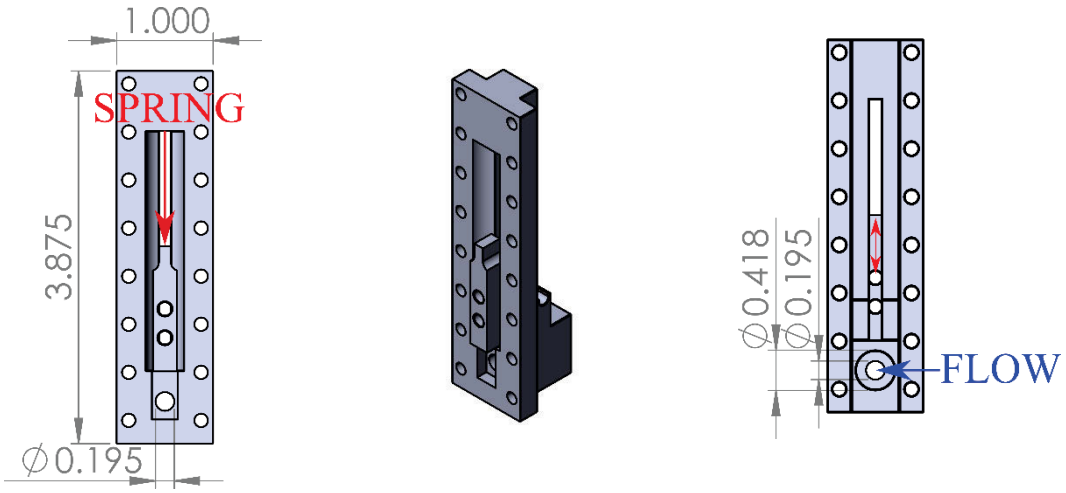


a) Internal view b) Isometric view c) External view

**Figure 4.5.** Gate-Valve Schematics. All Units in Inches.

observed to escape vertically through the plunger shaft, effectively reducing the recorded magnitude of any excited mode in a nozzle. As it concerned the 1T mode, this reduction in magnitude was deemed unimportant, as the captured phenomenon existed well above the noise-floor of the transducer. For other, weaker modes, this pressure loss had the potential to preclude accurate capture of data. This was indeed the case for the 1T1L mode, which—along with several other issues—forced efforts into capturing the decay of this mode to be abandoned.

## 4.2 Experimental Methodology

Three distinct experimental methods were utilized over the course of all testing in this work. The first involved sweeping the frequency over wide bands to first characterize the general frequency response of the test article in question, and then over much more narrow bands to isolate resonant frequencies. The second experimental method involved simply driving the test article at the identified resonant frequency in order to capture the acoustic behavior of the excited mode, and thus provide information to assist with mode identification. The third experimental method involved driving the chambers at the identified mode and—with the gate-valve installed—capturing the acoustic attenuation of

the excited mode upon valve closure. One crucial concern for all such methods involved the location of the transducers—for example, purely longitudinal behavior would be missed by a purely tangential arrangement. Once the decision was made to focus purely on the 1T mode, this was far less critical.

### *4.2.1 Frequency Characterization*

To perform the characterization sweeps, a set voltage range and increment were set in the control VI. Typically, sweeps were set with a 0.01 V increment, which ideally would correspond to 5 Hz increments in frequency. Due to the drift in the siren, however, this is more realistically reported as about a 10 Hz frequency increment. In order to practically sample at 40 kHz, the VI was coded to update and collect data every half-second. In other words, 20000 data samples are taken per voltage increment, where each increment persists for this half-second interval **[60]**. Initially, these frequency-response data were first analyzed with a basic FFT. However, as an FFT provides the average frequency content over the entire window, a single-window approach applied to the entire sweep did not provide precise data. To rectify this, a cumulative set of windowed FFTs (typically on the order of 1000), where each window is over approximately 0.5 seconds, were taken. Recall the siren resided at a constant frequency for 0.5 seconds before increasing by an increment—in this manner, each window corresponded to this constant frequency excitation period. In a previous work, the plot that results from this method was titled a cumulative fast-Fourier transform, or CFFT **[60]**. The CFFT can be viewed as a spectrogram where the time information lies normal to the page.

This cumulative plotting method provided a clearer perspective on the magnitude and precise frequency of any excited modes. Figure 4.6 provides two examples of a CFFT versus a standard FFT from one transducer mounted in the ER nozzle. The most immediate disparity in this figure arose from the reported magnitudes of both schemes. The reported magnitudes from the FFT are *well* below the reported magnitudes from the CFFT. The magnitude reported from the CFFT is more realistic than what is observed with the FFT. Another immediate disparity is observed between Figure 4.6c) and Figure 4.6d), insofar as

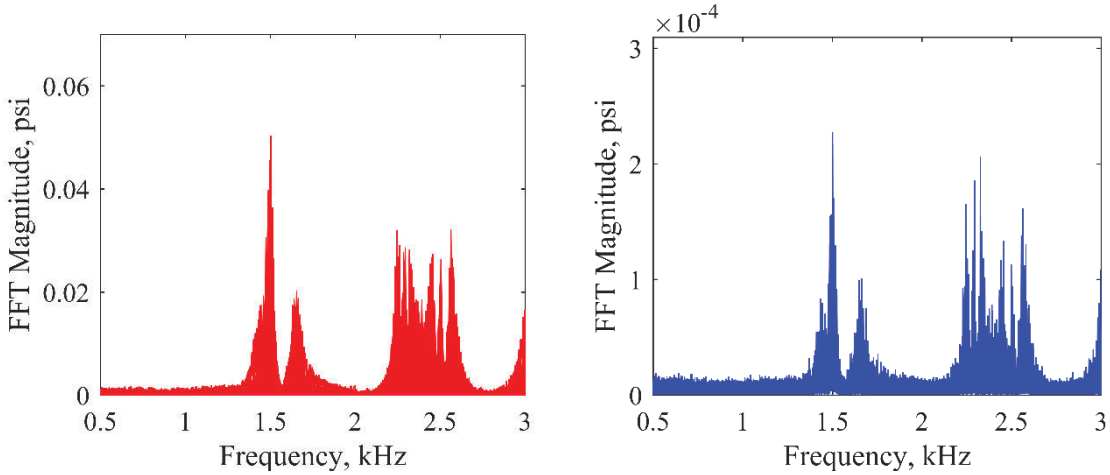


a) CFFT from 500 to 3000 Hz

b) FFT from 500 to 3000 Hz

c) CFFT from 1400 to 1600 Hz

d) FFT from 1400 to 1600 Hz

**Figure 4.6.** CFFT v. FFT Data from the ER Nozzle

the resonant frequency around 1500 Hz is concerned. The CFFT provided a clear, singular peak at 1500 Hz, whereas the FFT provided two peaks in the region around 1500 Hz. Recalling the averaging nature of the standard FFT, it is not clear then which peak should actually dominate. There was no such doubt with any CFFT plot, and hence that means of analyzing the frequency response of the test articles was found to be far more useful.

Figure 4.6a) depicts the frequency response of the ER chamber from a sweep over the range 500-3000 Hz. The observed peaks in the trace correspond to the resonant, acoustic modes that were excited when the driving frequency of the siren was at or very near the appropriate frequency. This image, then, serves as an example of the characterization granted by the frequency-sweep tests. However, from these data alone, it is not possible to concretely identify what mode corresponds to what frequency—this is the purpose of the second experimental method.

### *4.2.2 Frequency Identification*

To properly identify the resonant modes, the amplitude and phase data from each transducer per mode were necessary. Further, spatial information regarding the placement of the transducers were necessary. For example, consider the 1T and 1T1L mode. Supposing all else is held equal, and the magnitudes of the modes are similarly equal, a purely tangential configuration of transducers will yield the same, or approximately the same data. Longitudinal data are necessary to distinguish between the pure and mixed mode.

The data taken from the frequency-sweep tests are insufficient for the purposes of mode identification due to the change in frequency thereof. To obtain the necessary amplitude and phase data, the driving frequency must be held as approximately constant as realistically possible. In this experiment, intervals from five to three seconds of driven data were used for this purpose, though shorter intervals would similarly be sufficient. Longer tests provided a better averaging influence on anomalies and drift present for all tests, and thus mitigated contamination. The explicit numerical means of mode identification will be

discussed in the following chapter—for now, it is sufficient to claim that the phenomenon observed at 1500 Hz is the sought after 1T mode.

### *4.2.3 Frequency Attenuation*

The final experimental method involved the installation and use of the 3D printed gate-valve. As with the driven tests, the driven frequency was kept as constant as possible, and transducers were placed according to the mode under investigation. As it concerned the 1T mode, the transducers were placed into the pure tangential configuration. Each test was set for either three or five seconds, and the gate-valve was activated after a brief delay or approximately one second. The valve was hand-operated, meaning there was no true precision in the valve's time of activation. This is not a detriment, however. Ideally, immediately upon activation the resonant frequency in the nozzles would decay according to the exponential relationship defined in Chapter one, and depicted in Figure 2.1. To even observe this, however, required the development of several scripts and functions. A general overview of these are introduced in the following chapter.

# CHAPTER FIVE
# NUMERICAL METHODS AND DATA ANALYSIS

This chapter will provide details on the means used to analyze the data collected over the course of this experiment. The bulk of the analysis was concerned with isolating the frequency component from the raw signal of a transducer, and observing its behavior over time. This particular process will be explicitly demonstrated, as it represents the most crucial part of this work. All data analysis was done in MATLAB ver. R2016B.

## 5.1 Attenuation Analysis

The analysis begins by extracting the raw signal from the six transducers. Figure 5.1 depicts one such example collected during this work. Embedded in this signal lies all the necessary data to acquire an estimate of the decay rate for the excited mode. Note that exponential decay can already be observed in this figure. However, there is too much noise embedded in the signal as is to sufficiently determine a decay rate without significant

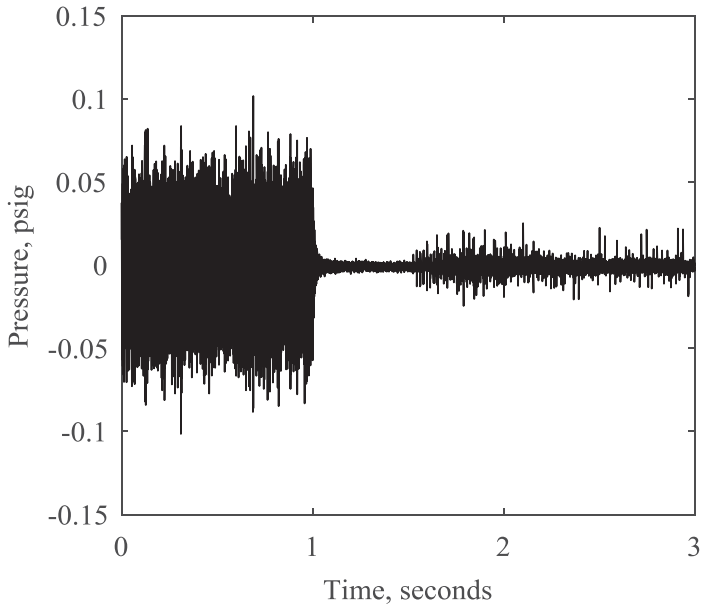


**Figure 5.1.** Raw Output at A in the ER Nozzle

corruption. To that end, it is necessary to filter the signal in a passband around the dominant frequency. To minimize the impact of the filter on the data, a 2nd order Butterworth filter with a ±20 Hz passband was chosen for this purpose. Other filter types, such as elliptical or Chebyshev—as well as higher orders—begin to numerically corrupt the input data. The passband was chosen to avoid introducing error into the observed decay rate—passbands of ±10 Hz or fewer acted as wide moving averages on the data, and significantly decreased the magnitude of the estimated decay rate.

Filtering was facilitated via MATLAB's built-in function *filtfilt*, which performs a zero-phase-distortion forward and reverse filter on the input signal. In the majority of cases, the result of the filter resembles Figure 5.2 in smoothness and shape. The exponential decay in Figure 5.2b) is precisely what damping theory predicts for acoustic decay. A detail to take note of is the oscillatory pattern in the red filter trace in Figure 5.2a), which remains embedded in the signal despite filtering. The driving mechanism behind this phenomenon lies in the siren drift—as the siren is not able to maintain a constant frequency, the pressure oscillations inside the chamber shift in and out of resonance just enough for the mean pressure to fluctuate. This can be visualized by referring back to Figure 4.6c), and noting

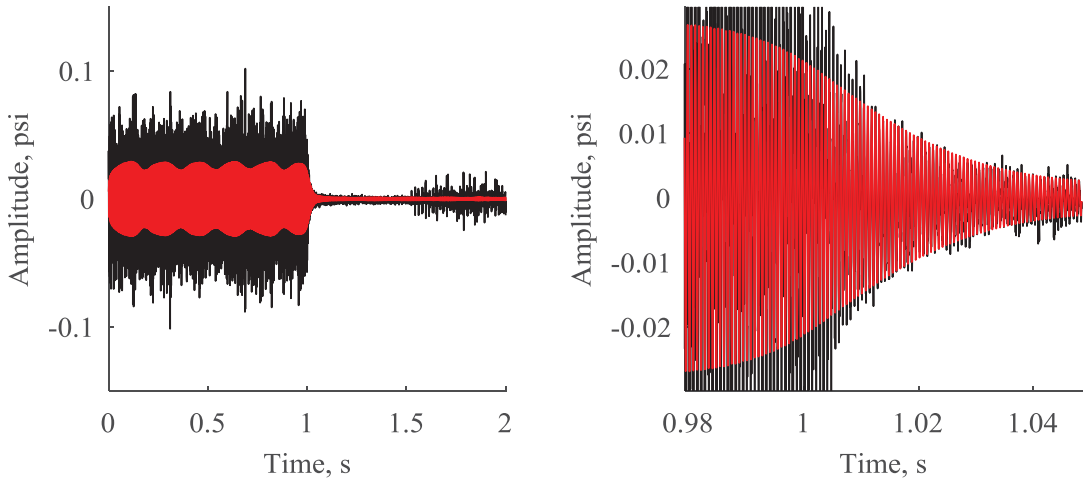


a) Raw output in black, and filtered signal in red.

b) Zoomed in view of the exponential decay.

**Figure 5.2.** Filtered Pressure Trace Showcasing Exponential Decay

the reduced magnitude of the CFFT in the near-region around the 1500 Hz peak. It must be noted that this may have some impact on the collected data—as it was not possible to remove or even mitigate this experimental factor, it was not possible to fully address the impact of this potential error. However, insofar as determining the decay rate was concerned, the closure of the valve isolated the chambers from ill-behavior in the siren. This can be observed by the lack of oscillatory noise in the exponential region and beyond.

Recalling Figure 2.1 and the theory of underdamped oscillations, it follows that the upper envelope of the filtered signal in the decay region is an exponential function governed by a decay rate, α. Hence, the upper envelope of the entire filtered signal is taken—determining the appropriate decay window similarly requires this envelope. To extract this analytic upper envelope, the function *envelope* was used. Figure 5.3 depicts the truncated output from this function.

One of the most crucial components of the analysis at this point falls under the selection of the decay window. A significant amount of effort was invested towards developing a repeatable, reliable means of isolating a region over which to further analyze.

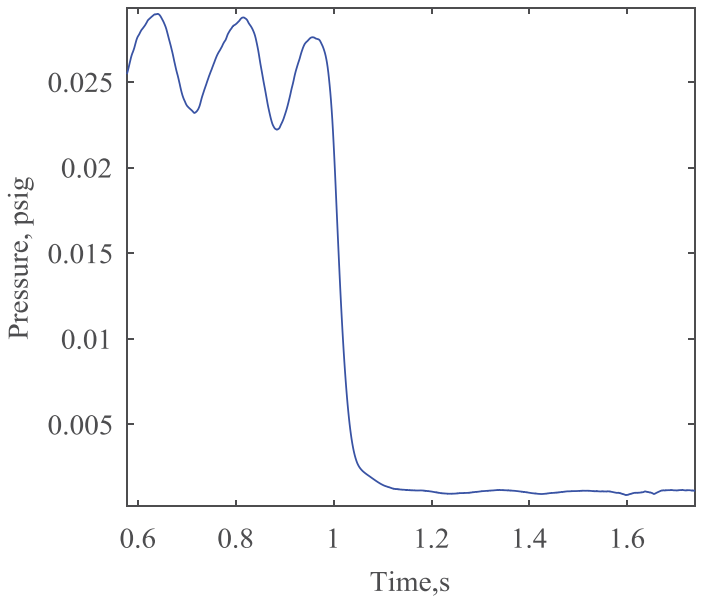


**Figure 5.3.** Upper Envelope of the Filtered Trace

Manual selection schemes, involving MATLAB's *ginput*—which permits a user to select points on a plot—were initially chosen for preliminary analysis. It was quickly discovered that resultant values for the decay rate were *extremely* sensitive to the lower and upper bounds of the specified decay window. Manual selection invited far too much inconsistency such that wildly different decay rates would be estimated between calculations. The initial solution involved the placement of a laser and photogate on either end of the gate-valve. This system was tied to the same data acquisition system as the transducers so that they ran on the same time vector. The ideal operation of this system yielded a lower bound on the decay window when the valve was fully closed. A script would then take the global minimum a user-specified distance away from the lower bound as the new upper bound of the window. This is the method reported and used in Price, et al **[60]**.

In general, this method produces fairly consistent results provided the operation of the photogate is ideal. In many cases, however, the photogate often failed due to misalignment or temporary blockage during the use of the gate-valve. Further, in order to mount this system, a severe length penalty was incurred in the siren-air deliver tube. The data contamination that resulted forced this method to be abandoned in favor of a numerical method for extracting the decay window. This scheme was as follows:

- The analytic envelope is passed into the function *findpeaks*. This function determines the local maxima of a given input, and returns the values and indices thus associated.
- The differences between the found maxima is computed via the *diff* function, which simply subtracts the nth peak value from the n+1 peak's value. This difference is theoretically greatest between the last peak before decay, and the first peak after decay.
- The indices of these bounding peaks are used to determine two time values, which then serve as the first-pass decay window.

At this junction, an important transformation was made. The natural log of the upper envelope of the filtered signal was taken. Recalling that the ideal behavior of the

decay is exponential, then the natural log thereof should be a linear function. An exponential model had three variables to fit, whereas a linear model only required two, and hence this transformation simplified the necessary analysis. From this transformation, the following was performed:

- The initial decay window is subdivided into 100 chunks. Thus, there were each 100 subsections of the time vector, and 100 subsections of the natural log of the upper envelope with which to work.
- A linear fit was applied to every data chunk, and the resulting slope was taken and recorded.
- The mean and standard deviation of these slopes were taken, and all chunks with a slope smaller in magnitude than the mean plus one-half the standard deviation were rejected. For example, if the mean slope is -20, and the standard deviation is 10, then all chunks with a slope of -15 or greater are rejected.
- A new decay window was established based on the lower and upper bounds of the surviving chunks. A refined linear fit was applied to this new window. Figure 5.4 depicts the output of this analysis, with the applied fit serving as an estimate for the decay rate, $\alpha$.

This method is sufficient for well-behaved decay. However, over the course of the experiment, there were several occasions where the recorded decay did not behave in this ideal manner. On these occasions, the aforementioned routine was insufficient in evaluating an appropriate $\alpha$. To address these outliers, a routine was coded that analyzed the coefficient of determination:

- For all test cases, a minimum coefficient of determination of 0.99 was imposed.
- If even one fit was below this minimum requirement, then the decay window for all arrays was set to the mean of the decay windows associated with the fits that passed this requirement. In general, this was a safe action, given that the decay should theoretically be approximately equal throughout the nozzle.
- If *all* fits failed to meet the requirement, then the new minimum coefficient of determination was set to the maximum $R^2$ of that file, and the decay window was

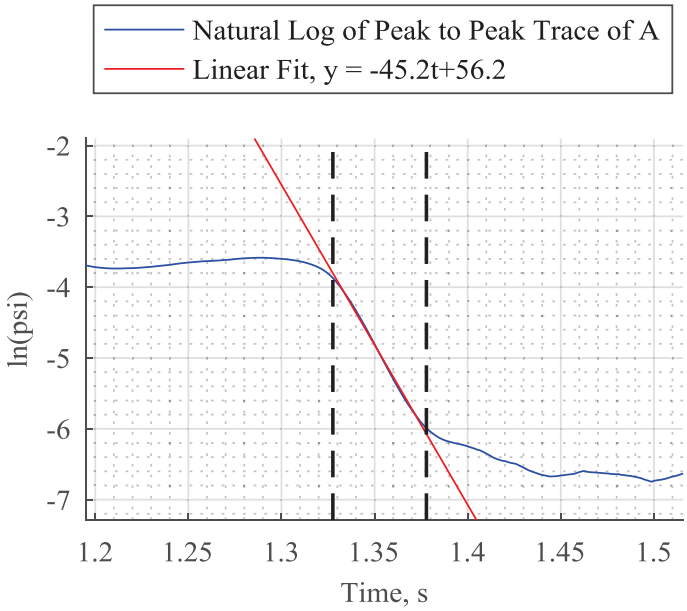


**Figure 5.4.** Linear Fit and Slope of the Natural Log of the Envelope at A

forcibly halved. This particular situation only emerged when the recorded decay was anomalous for all locations.

- The results from either IF statement were then passed back through the original fitting function outlined previously.

With these IF statements in place, the written scripts were able to effectively and consistently process all of the data collected in the present work.

## 5.2 Other Methods

### *5.2.1 Discrete Fourier Transform*

The use of the upper envelope can be substituted by taking the discrete Fourier transform (DFT) of the signal in question at the dominant frequency over many windows. The minimum window size for a DFT used in this application must encompass one period, and windows larger than this begin to act as averages over periods. In this manner, the amplitude over time of the frequency of interest can be obtained. An FFT may also be utilized, but the window size *must* be larger than one period. Further, the routine will likely

be much slower in computation than a DFT. Both schemes still necessitate the use of a filter of some kind to avoid producing erratic decay rates due to noise. The envelope method was selected over the DFT method because the DFT method required that the output array be some degree smaller than the input array. The envelope method preserved the array size, and thus provided a greater number of points over which to apply linear fits.

### *5.2.2 Mode Identification*

Mode identification was facilitated by two functions: one that yielded the cross-sectional shape of the mode inside the nozzle, and one that yielded the phase measured by the pressure transducers. Both provided the necessary evidence to identify tangential mode shapes. Note that, by the time these functions were designed, the decision to focus entirely on the 1T mode was made, and hence these functions were only valid for the 1T and other tangential mode shapes. Both functions required data taken from the frequency-specific driven tests, as the root of both functions was a DFT. From this DFT, the Fourier sine and cosine coefficients could be extracted by the following equations:

$$A_n = \frac{2}{NT}\int_0^{NT} p(t)\cos\left(\frac{2\pi tn}{NT}\right)dt \qquad \textbf{(5.1)}$$

$$B_n = \frac{2}{NT}\int_0^{NT} p(t)\sin\left(\frac{2\pi tn}{NT}\right)dt \qquad \textbf{(5.2)}$$

Here, $A_n$ and $B_n$ are the Fourier cosine and sine coefficients, respectively, which represents how strongly the correlated function, *p(t)*, matches a cosine or sine wave. These coefficients were used to determine the norm and phase of the input array—as each array corresponded to a different transducer at different locations, the norm and phase of each would be different owing to the shape of the excited mode. The quotient $\frac{n}{NT}$ represents the frequency, *f*.

A user-written script titled *nodecode* required as inputs the six normalized magnitudes from the DFT, and an array corresponding to the angular locations of all transducers. For all experimental runs involving the 1T, this array was 0, 70, 90, 115, 270, and 310 degrees. The normalized amplitudes from all six transducer arrays were again

normalized with respect to the maximum amplitude, such that the values span from zero to one. A set of angle and amplitude arrays over which to loop were created, with each point corresponding to a location on the cross-section plane created by the tangential transducer array. At each point, a new amplitude was computed by the following equation:

$$Y_{ij} = y_i\left|\cos\left(\theta_{transducer} - \theta_j\right)\right| \quad \textbf{(5.3)}$$

In this equation, $y_i$ corresponded to the iterative amplitude, and $\theta_j$ corresponded to the iterative angle. $\theta_{transducer}$ corresponded to a particular angle from the angular input array. Note that all angles in equation **(5.3)** are in *radians*. The output, $Y_{ij}$ was the new computed amplitude at a particular point on the cross-sectional plane, and was a number between zero and one. A least-squares analysis is performed between this computed amplitude and the twice-normalized amplitudes corresponding to actual transducer measurements. An amplitude output—which should be approximately equal to the input amplitude—and phase output were produced. Using the amplitude and phase data, a mode shape was developed, of which Figure 5.5 is an example. To interpret this plot, Figure 4.3 must be recalled. Figure 5.5 is a similarly oriented cross-sectional slice of the nozzle in question, with transducer locations appended to the outer rim of the circle. The normalized amplitude markers corresponded to the measurements provided by the transducers at each port. Based on the phase data extracted from *nodecode*, an antinode line and node line were drawn. The antinode line was drawn from the origin at the phase angle and $180^0$ plus the phase angle, and the node line was similarly drawn from the origin at $90^0$ plus the phase angle and the phase angle minus $90^0$. The two red circles were drawn based on the amplitudes, and in conjunction with the antinode and node lines, represent the theoretical shape of a 1T mode. Thus, the amplitude markers should ideally lie along the red circles for 1T excitation.

The next requisite piece of information to sufficiently conclude if the excited mode was a 1T mode involved the use of the phase angles from each transducer array. To accomplish, the phase angles were normalized by subtracting transducer array B's phase from the phases of all other arrays—this is because transducer B was persistently driven by oscillatory flow from the siren, and thus always possessed the largest amplitude in all experimental runs. Note that this choice is arbitrary—normalization by any other

transducer was sufficient. The real and imaginary components of the phase per array were determined by taking the cosine and sine of the phase angles, respectively, and multiplying them by the normalized amplitudes. Figure 5.6 provides an example of what this process developed. This plot provides information regarding the structure of the waveform captured by the transducers. In this example, markers A, B, and C are approximately 180° out of phase with markers D and E, meaning that if A, B, and C correspond to a peak in the waveform, D and E *must* correspond to a valley. With the exception of the marker labeled 1, the phase configuration presented in Figure 5.6 approximated the theoretical configuration that must be possessed by a 1T mode relative to the tangential transducer configuration.

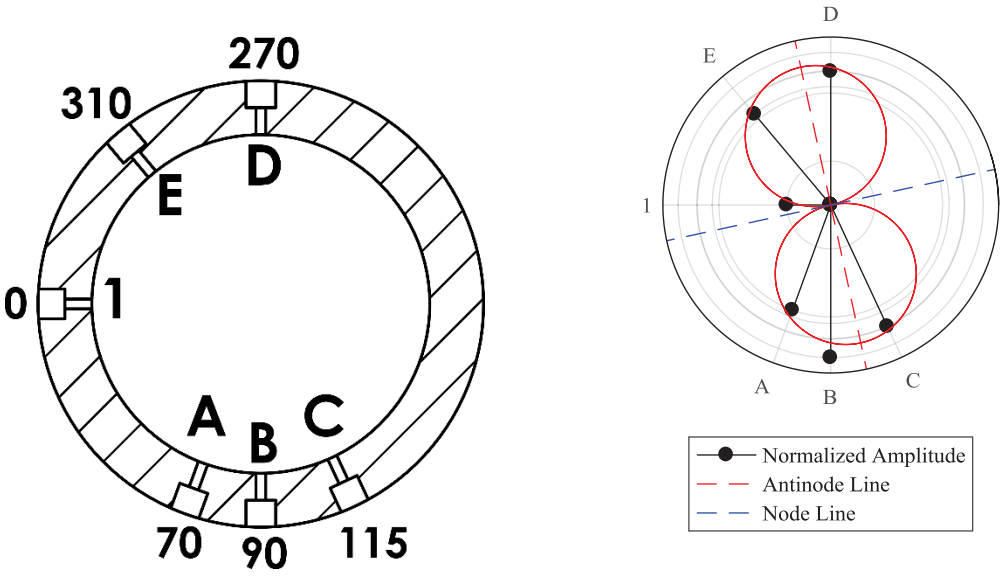


a) Nozzle cross section

b) Polar plot overlayed onto the nozzle cross section

**Figure 5.5**. Mode Shape Plot from the ER Nozzle with Cross Sectional Reference

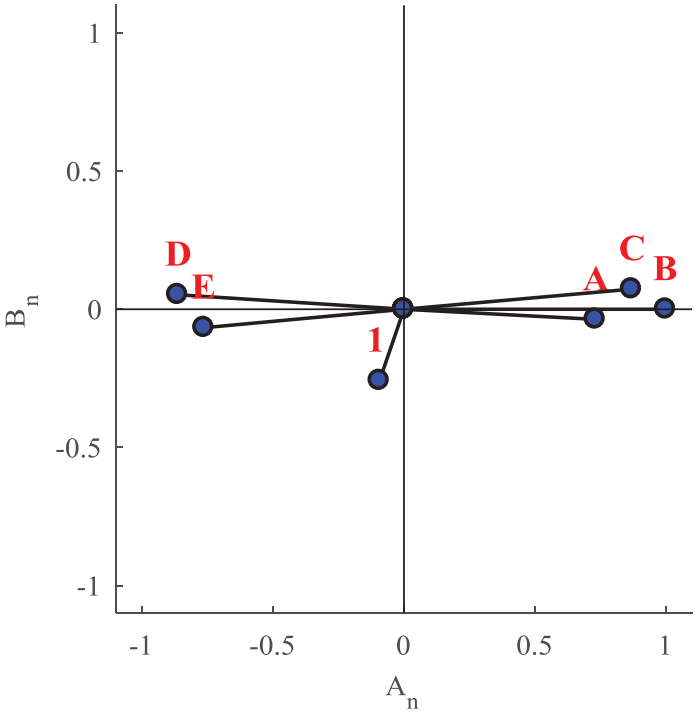


**Figure 5.6.** Phase Plot Example from the ER Nozzle

# CHAPTER SIX
# RESULTS AND DISCUSSION

Over the course of this experiment, a total of 314 experimental tests were performed. The bulk of the early experimental runs involved characterizing the frequency response of all three test-articles, and identifying potential modes to analyze. Attempts were made at analyzing the following modes: 1L, 2L, 1T, 1T1L, and the 1R. Of those, only the 1T1L and the 1T were feasible, owing the limitations of the equipment available in this experiment, with the most limiting factor being the acoustic capabilities of the siren. Of these two feasible modes, the 1T was the only mode for which attenuation analysis provided consistent, repeatable data. The principle cause of the inability to provide 1T1L data emerged from the geometry of the test nozzles and the position of the node lines for that mixed mode.

The most critical, missing component of the data presented in this work, however, involves the lack of mean-flow testing. All results presented in this work were taken without the presence of mean-flow choking the nozzles, and thus the acoustics are modified from what would be observed in an actual test flight. From a simplified perspective, the system is modified from a closed-closed acoustic system to a closed-open acoustic system. This absence can be entirely attributed to a lack of time and resources, and not to an inability of the available equipment to provide the necessary pressure. Regardless, the results collected in this work serve as an initial analysis of the geometry best suited for the dispersion of a 1T mode.

## 6.1 Frequency Characterization Results

Figure 6.1 depicts CFFTs of the frequency response for all three test geometries from 500 to 3000 Hz. The overall similarity between each nozzle was expected, owing to the geometrical similarity to which they were designed. The ER and conical nozzle in particular possessed approximately the same overall response, with the primary deviation resting within the pile-up of acoustic modes above 2000 Hz. The density of acoustic response in this region primarily arose from the truncated dimensions of the nozzles—

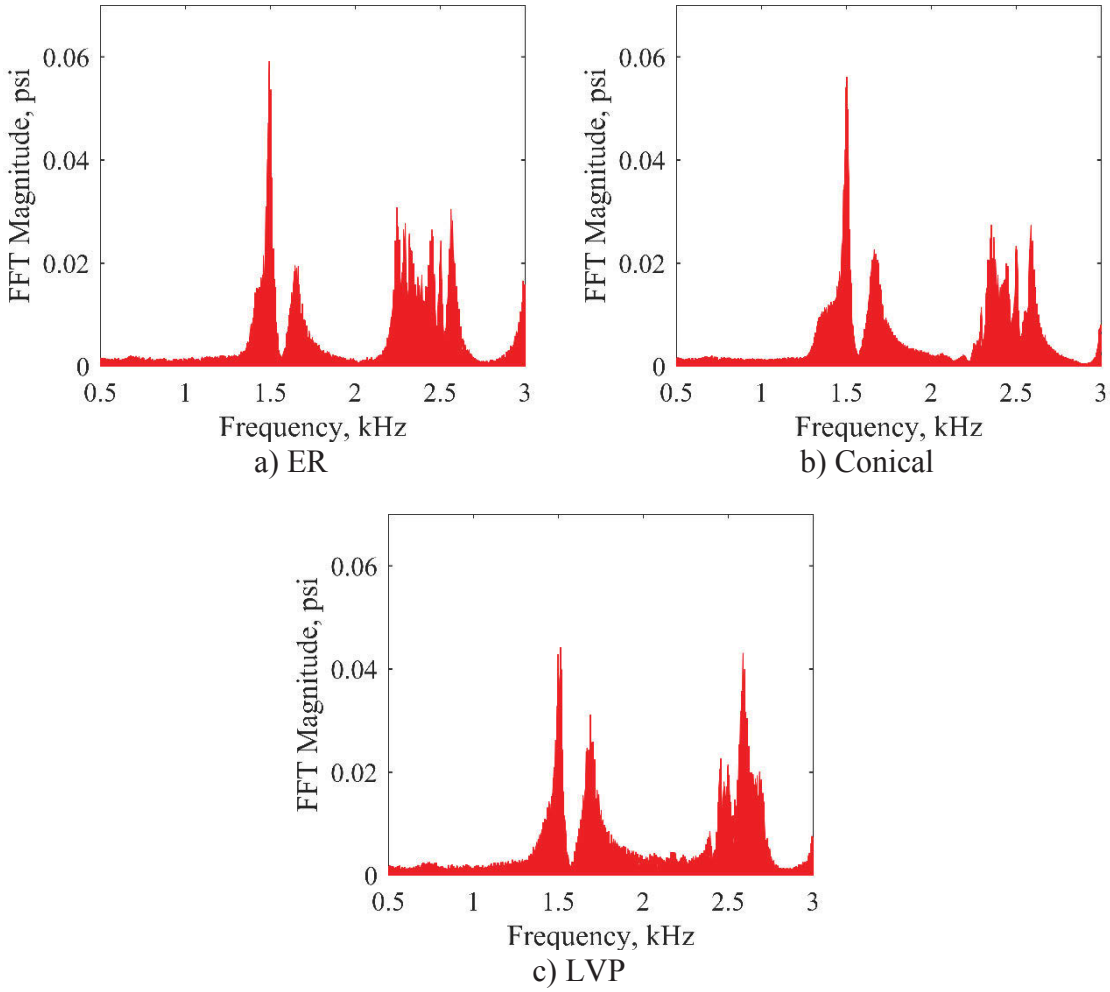


**Figure 6.1.** Frequency Response for All Nozzles at A

larger test sections would have tended towards a greater frequency-difference between modes. The response of the LVP nozzle was somewhat unexpected in that it noticeably diverged from the response of the other two nozzles. While the frequency content was approximately the same, the magnitudes were certainly different. Due to the small size of these nozzles, the interior acoustics were *extremely* sensitive to manufacturing defects, and it is believed that this was an influence on the deviation in the recorded magnitudes. Note that a statement about the damping of each nozzle cannot be made from analyzing the magnitude of the modes—while a reduced magnitude would point towards a damping influence preventing the growth of the mode, there are simply too many variables to reliably draw a conclusion based purely on that single metric. Such a metric is only reliable in the case that all acoustic parameters are equal between all cases—that is to say, that all node lines lie in the same planes; that all transducer ports lie at the same position for all nozzles; etc. Despite the best efforts to control experimental variation in this work, it will be shown that there still existed notable variation that defeats an analysis purely based on magnitude.

The peak at 1500 Hz corresponded to the 1T mode for all nozzles; evidence to this assertion will be given in a following section. The response at approximately 1650 Hz in all nozzles corresponded to the 1T1L mode—this assertion is less firm than the 1T declaration, and was made from an observation of mixed mode behavior, and that, in theory, the 1T1L should be the next mode after the 1T. Initial predictions as to the order of the acoustic modes were made based off of equation **(2.24)**, with one significant caveat. The derivation that led to the development of that equation assumed a closed-closed boundary condition. In accommodating the closed-open boundary condition, the following equation emerged:

$$\omega_{mnl} = a\sqrt{\left(\frac{\alpha_{mn}}{r_o}\right)^2 + \left(\frac{l\pi}{2L}\right)^2}\,, l = (2n-1)\;\forall\; n \in \mathbb{N} \qquad \textbf{(6.1)}$$

The critical difference between equations **(2.24)** and **(6.1)** is the division by two of the longitudinal component of frequency, and that $l$ is always odd. That is to say, there is

no 2L, 4L, etc. in a closed-open system. Note that, as before, this equation does not consider compressibility or divergences in geometry from a right-cylinder, and thus the reported frequencies from this equation were *radically* incorrect. However, this equation provided the *order* of the acoustic modes as they should emerge.

## 6.2 1L, 1R, and 1T1L Results

### *6.2.1 1L Results*

Referring back to Figure 6.1, note the lack of response below 1500 Hz. Theoretically, the 1L mode should have existed somewhere in the region between 400 and 900 Hz. However, in all testing, a peak in this region was never observed. There are two possible conclusions:

- The most likely result refers back to the issues with the siren, in that this frequency regime was simply too low to be adequately driven.
- If the assumption is made that driving was sufficient to excite a weak 1L mode, then damping was possibly so high as to heavily eliminate the mode.

The second assumption calls upon the coupling between the direction of longitudinal mode propagation and the direction of bulk flow in the nozzle **[11, 20]**. Note that "bulk" flow also accounts for flow from the siren, which must possess a mean longitudinal direction. A third conclusion is also possible: The transducers used in this work were not sensitive enough to capture 1L phenomena, and it is possible the 1 psig range variant may have been sufficient. Regardless, the low to nonexistent magnitude of the 1L would have presented a large problem in both mean flow and no-mean flow decay rate analyses—especially in mean flow testing, in which the noise of the bulk flow may have overpowered the acoustics of weakly driven modes.

### *6.2.2 1R Results*

More so than the 1L, 1R mode analyses suffered from the limitations of the experimental equipment. For the geometries used in this experiment, the 1R mode was predicted to be at or above 3000 Hz. However, recall Figure 4.1, which clearly

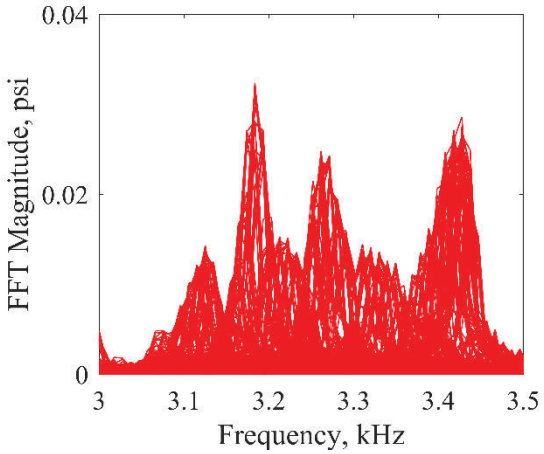


**Figure 6.2.** Frequency Response of the Conical Nozzle from 3000 to 3500 Hz at A

demonstrates that the pneumatic siren struggles to produce a discrete frequency in this range. Further, radial modes are *extremely* sensitive to imperfections in the circular cross-section of a cavity, and—owing to the pits and bumps that lingered in the nozzles after post-production—it is thus unlikely a 1R mode could be reliably driven. Figure 6.2 shows the recorded response of the conical nozzle at A (recall Figure 4.3) when the siren swept from 3000 to 3500 Hz, and is indicative of the response in the other two nozzles. While there was indeed a number of discrete peaks, these were far more likely to be tangential and mixed longitudinal-tangential modes, rather than any radial mode. Regardless, the unimportance due to the shape and rarity of the 1R mode relative to the 1T and the 1T1L mode drove a decision to abandon the search for the 1R.

### *6.2.3 1T1L Results*

Recalling Figure 6.1, it follows that the 1T and the 1T1L modes suffered none of the identification problems associated with the 1L and 1R modes. However, the reduced magnitude of the 1T1L mode relative to the 1T mode was significant in the present work, and was one of several factors that forced a retreat from analyzing the attenuation of this mode. Figure 6.3 shows the upper envelopes recorded in each nozzle by all six transducers in a mixed configuration. Note that the low magnitudes recorded were approximately half

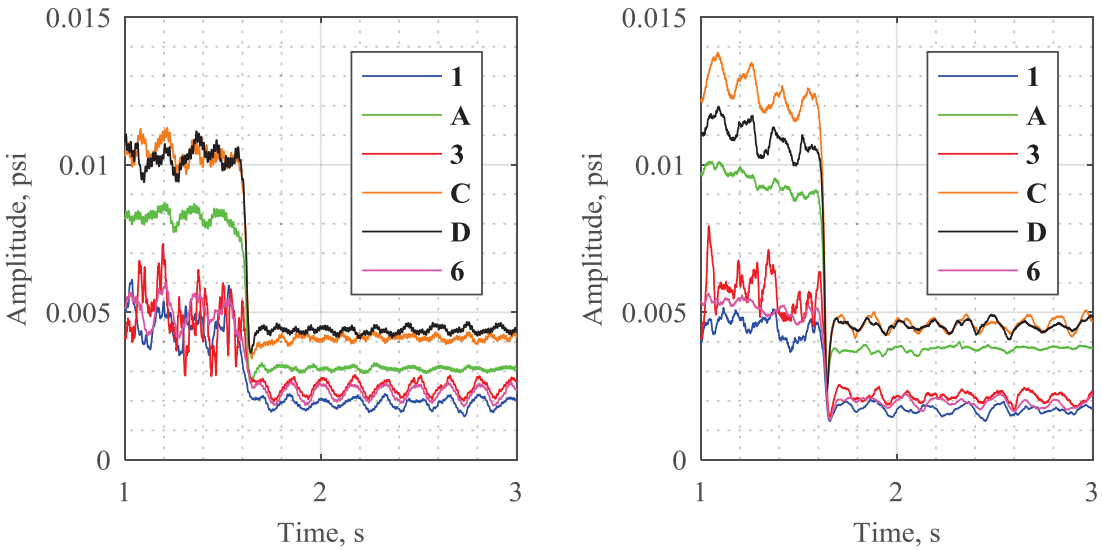


a) ER b) Conical

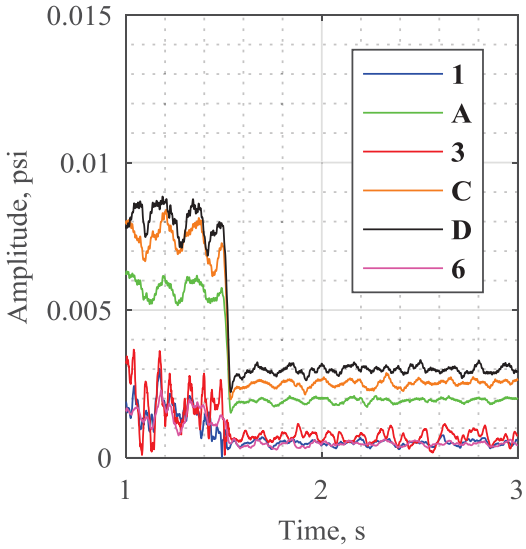


c) LVP

**Figure 6.3.** 1T1L Attenuation

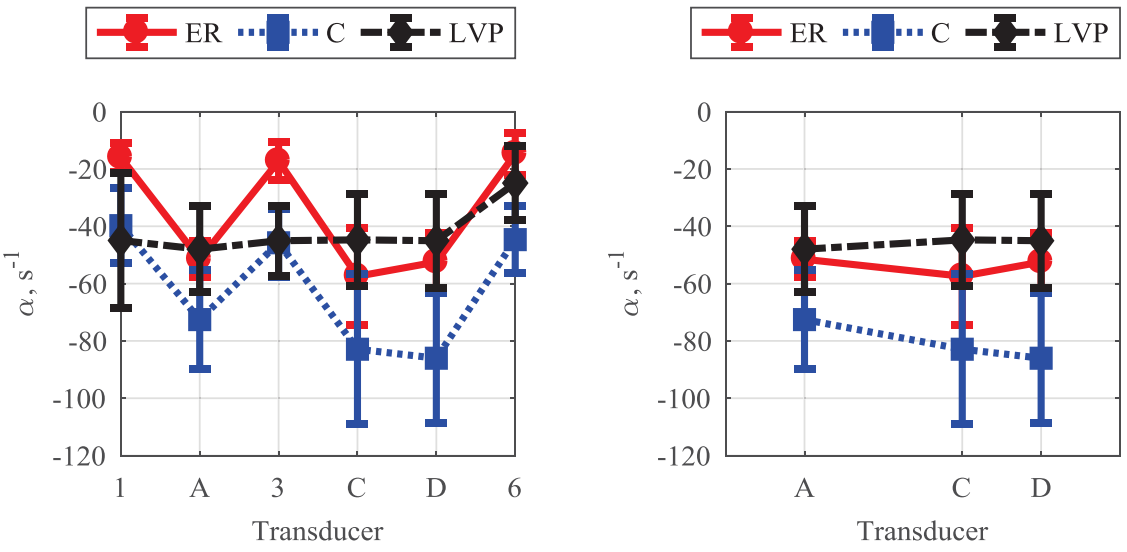


a) 1T1L data from all transducers

b) 1T1L data from only tangential transducers

**Figure 6.4.** Preliminary 1T1L Results

the magnitudes recorded in Figure 6.1–this emerged from the installation of the gate-valve, along with the photogate, which these early tests used. Note the extremely low magnitude recorded at locations 1, 3, and 6 in all tests, and recall that these were longitudinal locations.

Thus, the longitudinal row of transducers recorded a significantly lower pressure response than the remaining tangential transducers—this was key evidence early in the experiment that a node line had fixed itself near this location for each nozzle. The quality of the tangential recordings, however, were not much better, and tended towards inconsistency as far as fitting a linear decay rate was concerned. Figure 6.4 has plotted the results of five 1T1L tests per nozzle with a 95% confidence interval. In general, no significant conclusions can be drawn from the data, with the exception that the conical nozzle *may* provide more damping than the other two nozzles. This assertion is in line with the data taken by Janardan, et al., in which the conical nozzle provided the most 1L damping **[1]**. It is possible that the 1L component of the mixed 1T1L forced a similar trend to emerge here, but without additional, consistent data, this can only be an assertion.

The principle limitations to acquiring consistent 1T1L data involved the node line that established itself at the longitudinal array, and the pressure losses imposed by the gate-valve and photogate length penalty. Without significant modification to the current experiment, these could not be addressed. Indeed, the rejection of the photogate and the placement of the gate-valve next to the test articles may restore enough pressure to acquire consistent results with the tangential transducers. To address the node line, the test article could simply have been rotated. However, as the 1T mode dominated all concerns with regards to importance, these modifications were left as ancillary goals if time had provided.

## 6.3 1T Results

### *6.3.1 Mode Shape and Phase Plots*

Nondimensional phase and amplitude data for each nozzle under 1T excitation are given in Table 6.1. Note that these data are similar to data published in Price, et al **[60]**, which can be viewed as a preliminary study to the data recorded in the present work. This table contains the necessary information required to declare the 1500 Hz acoustic mode as the 1T mode. These data are depicted graphically in Figure 6.5 and Figure 6.6, which contain the mode shape plots and phase plots, respectively. The fit of the markers in Figure 6.5 to the theoretical, red circle, and the approximately 180 degree separation between transducers across the blue node line in Figure 6.6 provided significant evidence towards the identification of this mode, coupled with initial estimates which predicted this mode between 1400 and 1550 Hz. One key observation to make with these data is that the data

**Table 6.1. Nondimensional Amplitude and Phase Data**

| **Mode: 1T** | Nondimensional Amplitude Transducer | | | | | | Nondimensional Phase Transducer | | | | | |
|---|---|---|---|---|---|---|---|---|---|---|---|---|
| Nozzle | 1 | A | B | C | D | E | 1 | A | B | C | D | E |
| ER | 0.275 | 0.732 | 1.000 | 0.873 | 0.865 | 0.766 | 1.000 | 0.014 | 0.025 | 0.044 | 0.713 | 0.746 |
| C | 0.392 | 0.740 | 1.000 | 0.860 | 0.920 | 0.706 | 0.977 | 0.371 | 0.361 | 0.351 | 1.000 | 0.999 |
| LVP | 0.166 | 0.716 | 1.000 | 0.883 | 0.939 | 0.782 | 1.000 | 0.001 | 0.008 | 0.010 | 0.806 | 0.824 |

from location 1 were heavily influenced by the presence of a node line in close proximity, and that this trend persisted for each shown test.

In general, this condition persisted for *all* experiment runs, due to the geometry of the chambers. The primary culprit locking the mode shapes into this constant behavior was the location where oscillatory flow entered the chambers—the node line thus set up approximately ±90° from this position. This similarly occurred for all 1T1L tests, but due to the tangential configuration of transducers for 1T testing, this phenomenon was far less detrimental. It was for this reason that all information from location 1 was rejected in Price, et al. **[60]**—it has no merit, as there was little pressure fluctuation at that location. It will be shown that the pressure envelope at this location is barely above the noise floor, and hence suffers significant corruption. This is similarly depicted by the phase plots, where location 1 is an outlier barely any distance from zero.

### *6.3.2 Envelope Analysis*

Similar information regarding amplitude distribution can also be gleaned from examining the differences in the upper envelopes recorded from each location. Figure 6.7 depicts this for all three nozzles. Immediately apparent is the influence of the node line for the conical nozzle, in which location 1 experienced little change following valve-closure. This is reflected in Figure 6.5b), where the node line was almost aligned with location 1. The decay of location 1 in the LVP nozzle was also heavily influenced by being close to the noise floor, as can be observed from its prolonged decay relative to the other locations. Figure 6.7 also provides some hint towards the location of the antinode line, as locations B and D tended to possess the largest amplitude. Recall that these transducers were closest to the antinode line as prescribed by the theoretical shape of the 1T mode. Similarly, A and E tended to be the furthest away from the node line (excluding 1), and hence the recorded magnitudes at both locations were the lowest, location 1 notwithstanding. Figure 6.7 is indicative of the general behavior observed in all attenuation tests, with a few key exceptions. These, however, are far better viewed after being transformed by the natural

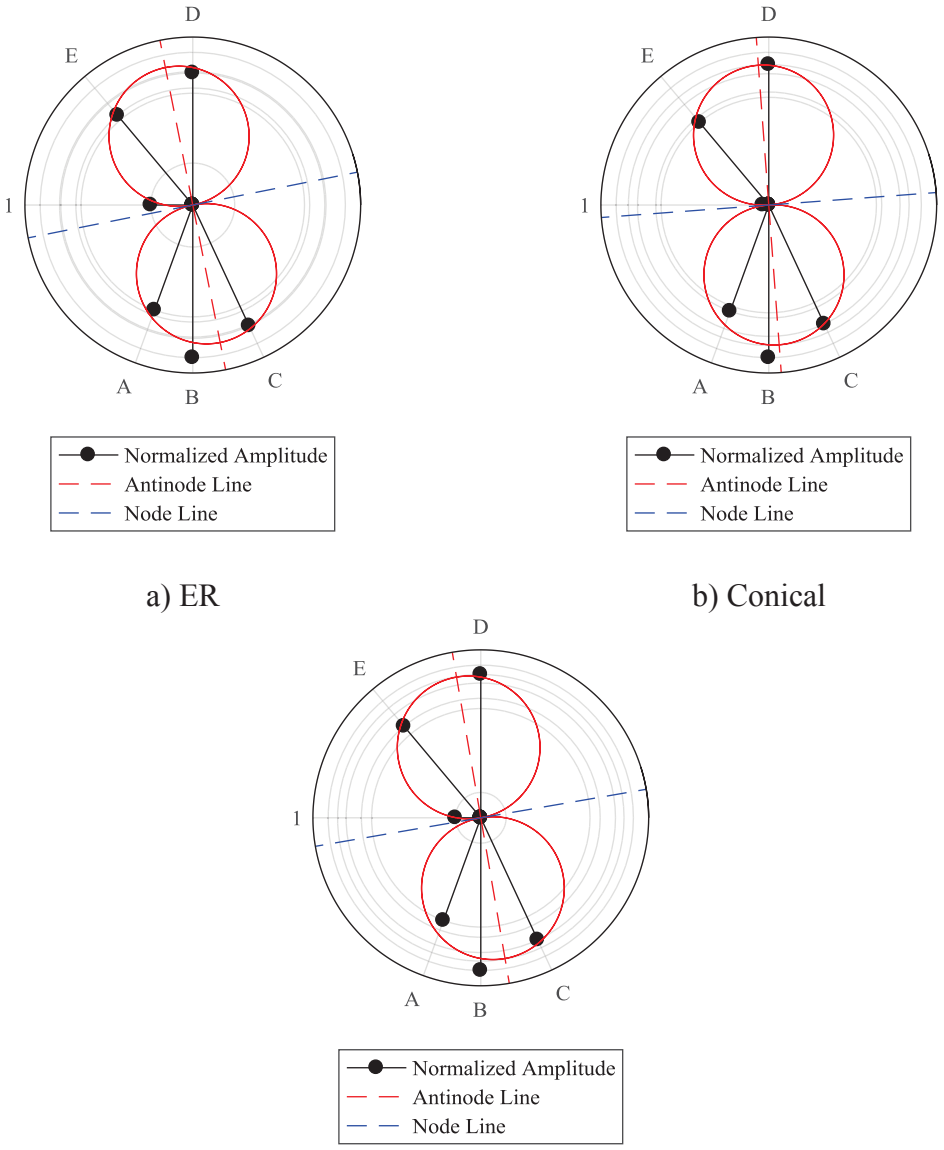


a) ER

b) Conical

c) LVP

**Figure 6.5.** Amplitude Distribution for Each Nozzle

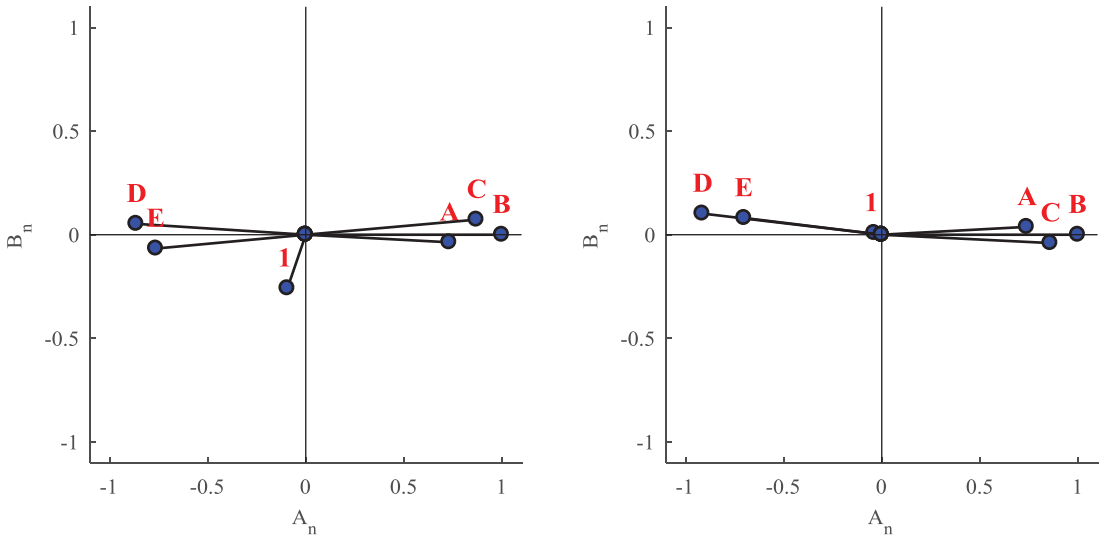


a) ER b) Conical

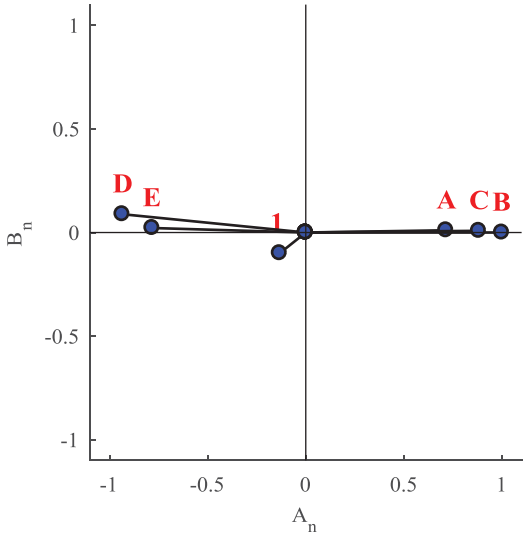


c) LVP

**Figure 6.6.** Phase Distribution for each Nozzle

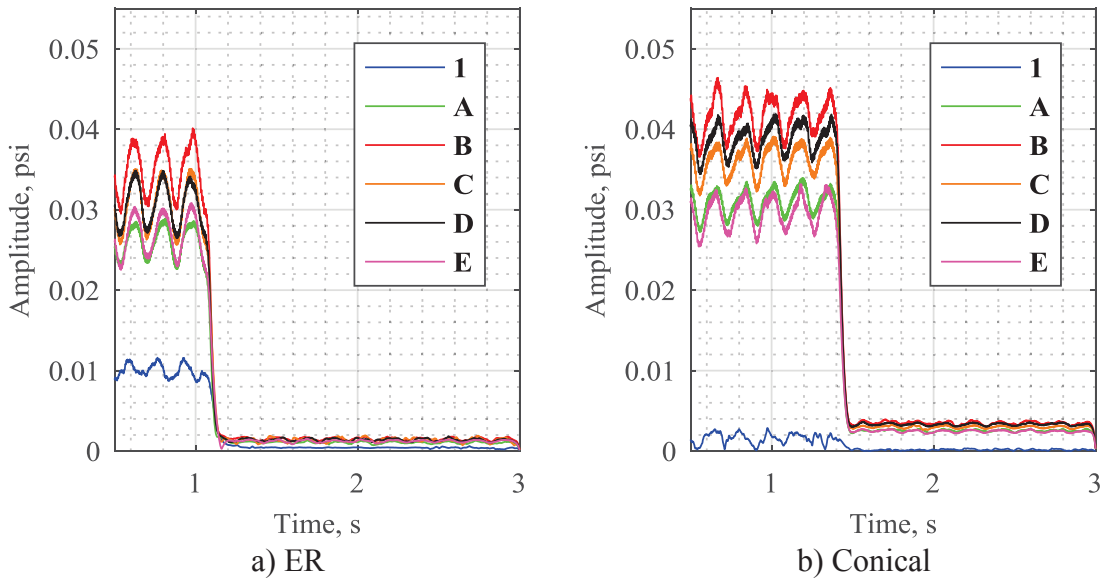


a) ER b) Conical

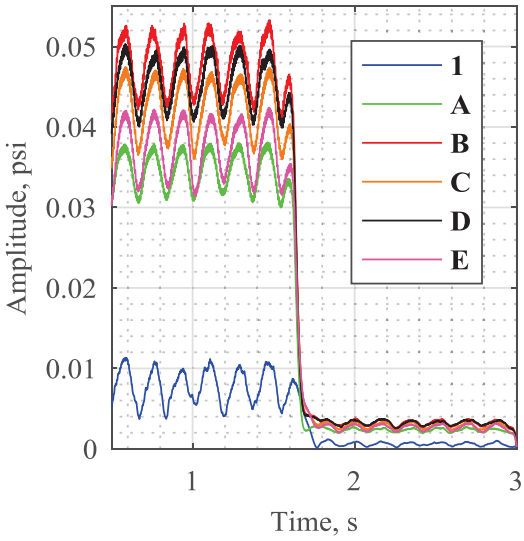


c) LVP

**Figure 6.7.** 1T Decay

logarithm. The wild oscillations observed before valve-closure emerged from the siren's unstable behavior, and could not be removed or filtered without unnecessary influence on the structure of the decay region. The absolute ideal situation would instead involve two linear regions before and after the exponential decay. Note that, in some cases, the oscillatory behavior was significantly reduced relative to what is shown—however, this in general was unpredictable.

### *6.3.3 Linear Fitting*

All of the estimated decay rates were extracted from the linear fit of the natural log of the upper envelope within the computed decay window for each location. Figure 6.8, Figure 6.9, and Figure 6.10 provide an example of the fits from each transducer in the ER nozzle, the conical nozzle, and the LVP nozzle, respectively. One immediate result from all three figures is the deviation in behavior from the norm committed by the trace recorded at location 1. Again, this is a result of the corruption from the noise floor permitted by the node line. Another key result that is hinted at is an order of most to least damping relative to the nozzle geometry. The ER nozzle appears to dominate 1T damping relative to the conical and LVP nozzles. However, such a conclusion cannot be properly deduced from one test per nozzle. These figures are indicative of the typical behavior encountered during all tests performed over the course of the experiment.

One particular type of anomaly existed in several test files that resulted in severely sharpened decay rates. These decays were "non-linear" in the sense that, after the natural logarithm had been taken, the resulting decay still maintained some degree of curvature. Figure 6.11 provides one such example of this "non-linear" decay. One thing to observe is the possibility of multiple linear fits. Fits made near the beginning of the decay were vastly different than fits made near the end of the decay, which steepens dramatically. In general, however, it was discovered that rejecting the latter half of this decay from the decay window introduced an estimate for alpha on the order of the average of other, non-anomalous estimates. The source of this anomaly is unknown. A *theory* has been formulated that, due to imperfections in the nozzle, there existed two 1T frequencies within

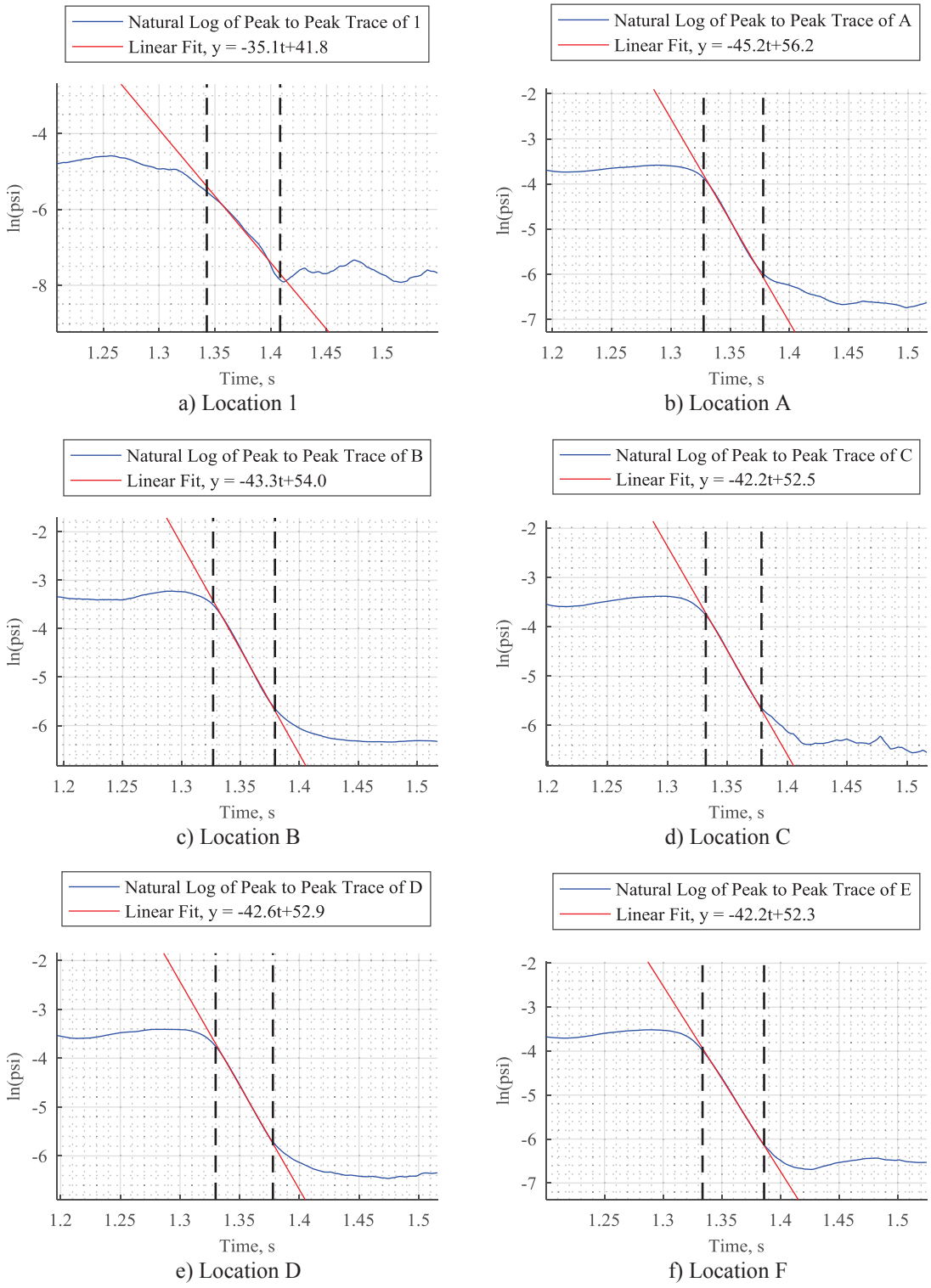


**Figure 6.8.** ER Nozzle Linear Fits

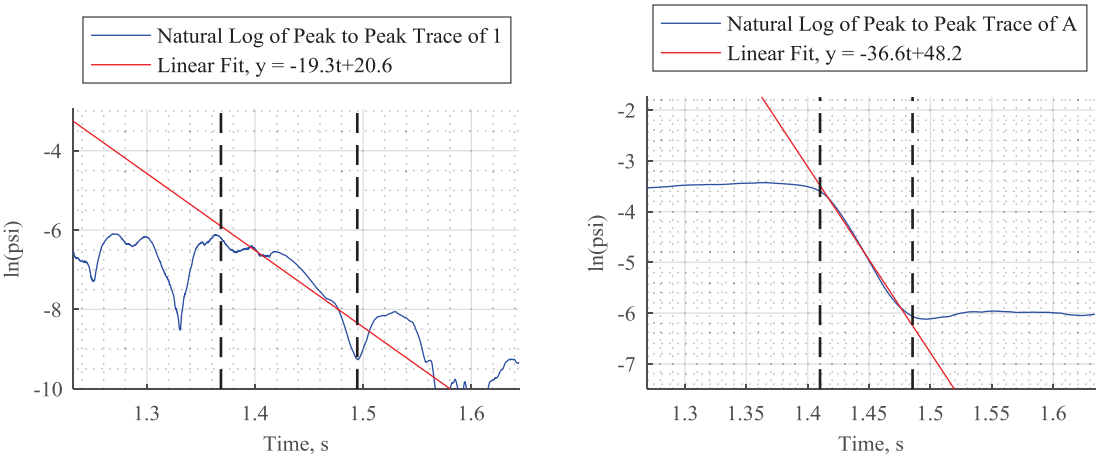


a) Location 1




b) Location A

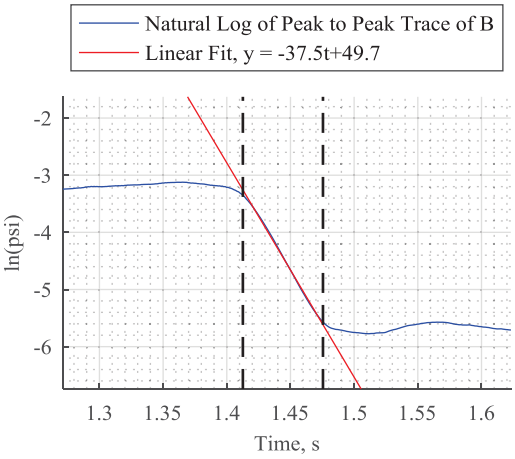


c) Location B

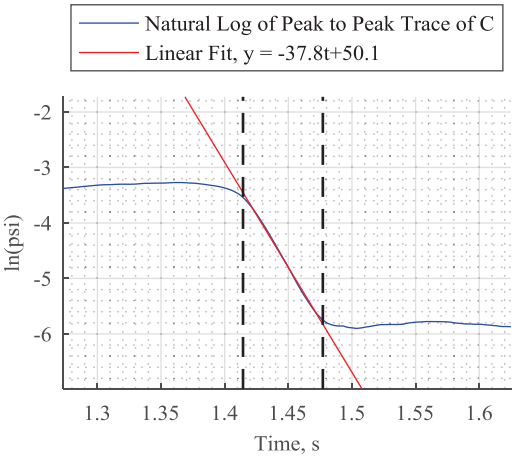


d) Location C

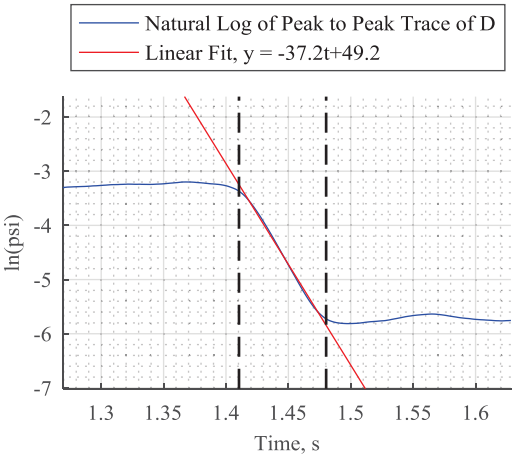


e) Location D

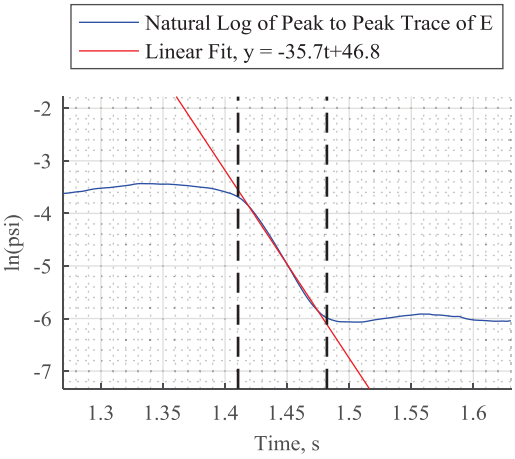


f) Location F

**Figure 6.9.** Conical Nozzle Linear Fits

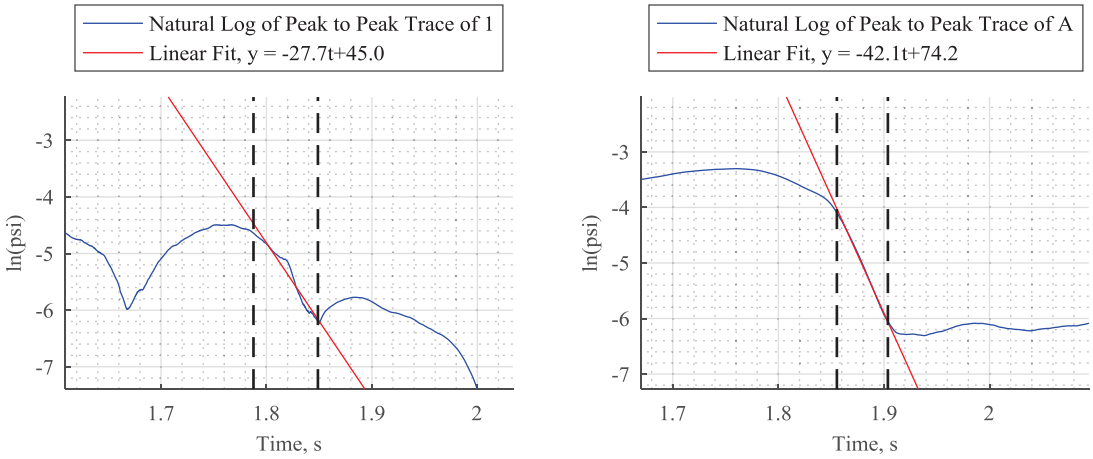


a) Location 1




b) Location A

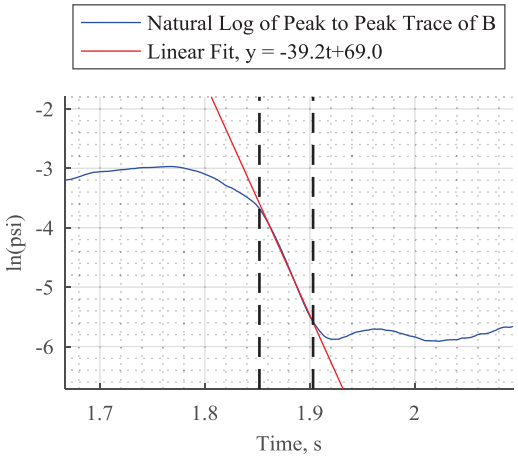


c) Location B

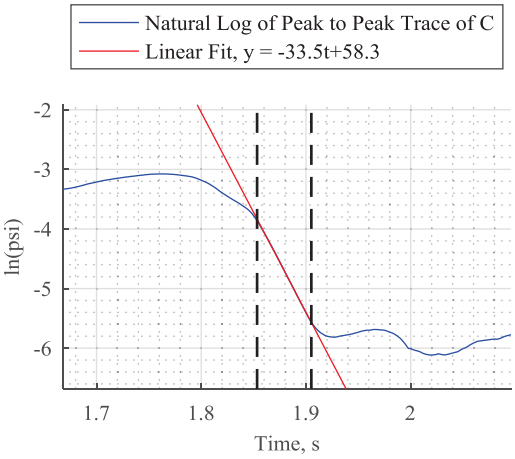


d) Location C

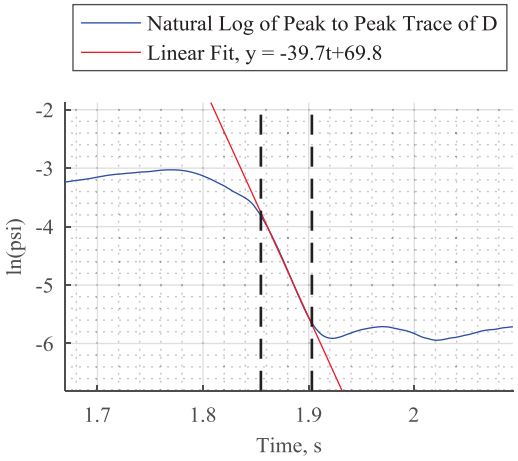


e) Location D

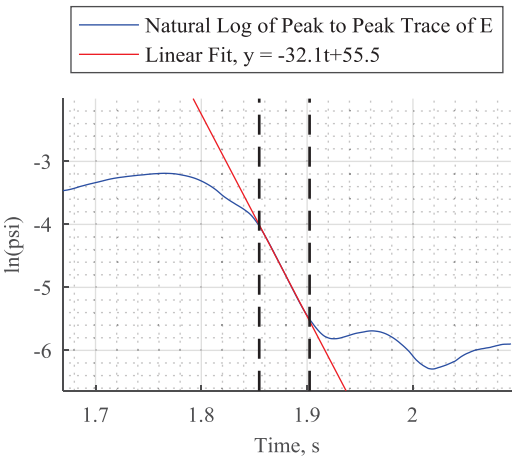


f) Location F

**Figure 6.10.** LVP Nozzle Linear Fits

several Hertz of each other, and this decay was a coupled interaction between these two frequencies. This anomaly must be acoustic in origin, as there existed several test runs where only one or two transducers at most observed this anomaly. That is to say, this behavior was not common to all locations when it did manifest, which makes it less likely to be rooted in the operation of the gate-valve or siren. That is not to say that there were not experiments where this behavior was common to all locations—three such experiments with the conical nozzle observed this anomaly at all locations.

An interesting observation can be made with this anomalous decay. The pressure in the nozzle rose after dipping sharply. The existence of any pressure in the nozzle following valve closure is ultimately due to the imperfect seal of the valve, but this pressure is on the order of 0.005 psig. This is the value to which the pressure returns to after the sharp valley; however, this raises a question regarding the origin of this notable drop in pressure. Without a simulation of some kind, it is difficult to ascertain any mechanism that could induce this phenomenon, but it absolutely must be noted that this anomaly can potentially disrupt attempts to apply linear fits consistently.

### *6.3.4 Decay Rate Findings*

Data from 15 attenuation tests per nozzle are available in Table 6.2, Table 6.3, and Table 6.4 for the ER, conical, and LVP nozzle, respectively. In general, all experiments

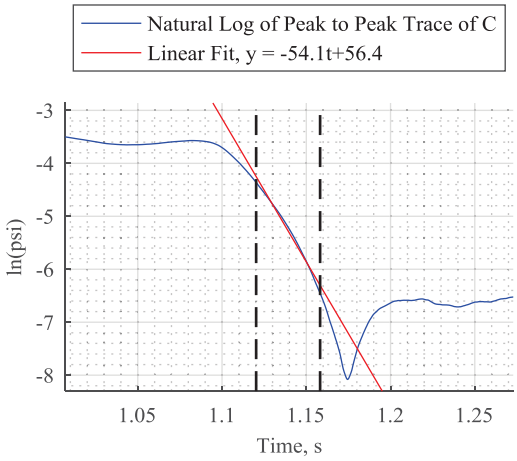


**Figure 6.11.** Anomalous Decay in the ER Nozzle at C

involving the 1T boasted superior consistency and repeatability relative to all other modes, which emerged from a number of factors:

- 1500 Hz was within the range of frequencies best excited by the siren.
- The 1T was the most prominent and easily excitable mode for each chamber.
- The inevitable node line only influenced one transducer of six, leaving five transducers able to capture accurate decay rate data.

Figure 6.12 condenses the data from the previous three tables by the mean alpha computed at each location, with one standard deviation above and below plotted. Note the relatively linear behavior of the conical and ER nozzle trends relative to the LVP's non-linear trend. In general, the LVP nozzle was less well-behaved than the other nozzles. Recall that in Figure 6.1, the LVP nozzle similarly diverged from the behavior of the ER and conical nozzles. It is likely there existed a manufacturing defect that influenced the disparity in behaviors thus observed. From the deviation plotted, it can be inferred that the mean decay rate of the LVP nozzle should probably be around -30 inverse seconds—locations C and E are both at this mark with little deviation around them relative to the other transducers.

It must be noted that these data conflict with data previously published in Price, et al. **[60]**. In that paper, the results published utilized the photogate, with all the issues previously discussed included. Further, only five tests per nozzle were conducted, and of those, only four were consistent enough to report. In this work, fifteen tests per nozzle were reported, and each was consistent enough to preclude exclusion. The damping rates computed in Price, et al. **[60]** under predict the damping of the 1T mode in each nozzle by varying degrees: The ER nozzle is off by 10 inverse seconds; the LVP nozzle is similarly off by about 10 inverse seconds; and the conical nozzle is off by approximately 30 inverse seconds. The behavior of the conical nozzle at the time those results were published was anomalous relative to the behavior now discussed, and likely had something to do with the gate-valve being about one foot from the chamber wall.

**Table 6.2. ER Nozzle Decay Rates**

| Transducers | | | | | |
|---|---|---|---|---|---|
| **1** | **A** | **B** | **C** | **D** | **E** |
| -26.97 | -53.32 | -45.44 | -46.33 | -47.27 | -47.48 |
| -37.74 | -44.87 | -38.63 | -35.65 | -38.85 | -38.91 |
| -28.82 | -43.15 | -38.69 | -38.34 | -38.18 | -37.13 |
| -29.95 | -53.55 | -52.16 | -48.50 | -51.52 | -52.21 |
| -25.37 | -52.70 | -51.55 | -47.88 | -51.17 | -47.39 |
| -25.06 | -31.90 | -33.36 | -35.25 | -33.07 | -35.58 |
| -23.64 | -41.54 | -38.58 | -34.57 | -39.71 | -39.24 |
| -25.73 | -48.48 | -48.76 | -53.25 | -48.94 | -53.30 |
| -38.77 | -42.51 | -39.94 | -37.66 | -38.86 | -36.62 |
| -30.19 | -45.19 | -48.39 | -53.92 | -47.44 | -57.15 |
| -27.86 | -48.13 | -50.01 | -53.99 | -48.13 | -56.00 |
| -28.98 | -54.86 | -56.81 | -58.93 | -54.33 | -58.94 |
| -29.84 | -45.18 | -43.29 | -42.24 | -42.57 | -42.17 |
| -23.68 | -54.28 | -56.18 | -57.79 | -52.98 | -58.03 |
| -25.92 | -56.41 | -60.16 | -76.33 | -58.03 | -56.95 |

**Table 6.3. Conical Nozzle Decay Rates**

| Transducers | | | | | |
|---|---|---|---|---|---|
| **1** | **A** | **B** | **C** | **D** | **E** |
| -15.05 | -41.36 | -42.11 | -41.37 | -41.37 | -40.72 |
| -19.35 | -36.64 | -37.51 | -37.84 | -37.21 | -35.73 |
| -51.94 | -49.54 | -50.09 | -51.90 | -49.26 | -50.29 |
| -37.31 | -38.79 | -38.84 | -39.50 | -39.83 | -39.27 |
| -23.17 | -37.07 | -37.45 | -38.00 | -37.50 | -37.59 |
| -27.45 | -37.84 | -38.67 | -39.62 | -39.05 | -38.69 |
| -41.10 | -41.02 | -41.60 | -42.74 | -40.79 | -40.15 |
| -14.41 | -40.07 | -38.39 | -39.74 | -38.79 | -38.54 |
| -11.23 | -44.66 | -44.11 | -45.05 | -44.21 | -43.88 |
| -23.54 | -36.85 | -37.64 | -37.24 | -37.94 | -37.42 |
| -24.93 | -36.60 | -37.25 | -36.82 | -36.76 | -36.03 |
| -29.35 | -46.79 | -47.51 | -51.75 | -51.24 | -58.19 |
| -45.55 | -34.79 | -35.37 | -35.81 | -35.04 | -36.42 |
| -24.40 | -38.25 | -37.99 | -38.55 | -39.57 | -38.12 |
| -61.82 | -42.70 | -41.98 | -40.74 | -43.22 | -40.39 |

**Table 6.4. LVP Nozzle Decay Rates**

| Transducers | | | | | |
|---|---|---|---|---|---|
| **1** | **A** | **B** | **C** | **D** | **E** |
| -14.46 | -49.76 | -40.36 | -32.57 | -41.68 | -29.72 |
| -11.59 | -46.64 | -39.28 | -33.36 | -40.67 | -30.39 |
| -27.67 | -42.13 | -39.18 | -33.54 | -39.66 | -32.08 |
| -20.68 | -33.65 | -30.53 | -26.53 | -30.72 | -25.34 |
| -10.65 | -44.37 | -36.77 | -32.33 | -38.24 | -29.08 |
| -7.02 | -48.64 | -42.53 | -33.81 | -41.52 | -30.68 |
| -11.05 | -31.48 | -29.00 | -27.18 | -29.16 | -25.80 |
| -11.27 | -40.67 | -34.97 | -30.26 | -35.00 | -27.78 |
| -15.65 | -31.46 | -29.69 | -27.98 | -29.83 | -25.92 |
| -12.01 | -40.32 | -34.93 | -29.44 | -35.36 | -27.34 |
| -27.44 | -45.34 | -39.97 | -34.23 | -40.24 | -30.51 |
| -7.91 | -45.24 | -39.33 | -33.07 | -39.72 | -29.83 |
| -14.64 | -31.31 | -28.92 | -27.29 | -28.90 | -25.30 |
| -16.76 | -34.96 | -32.09 | -28.03 | -32.39 | -26.31 |
| -10.25 | -32.80 | -31.43 | -29.14 | -31.68 | -28.04 |

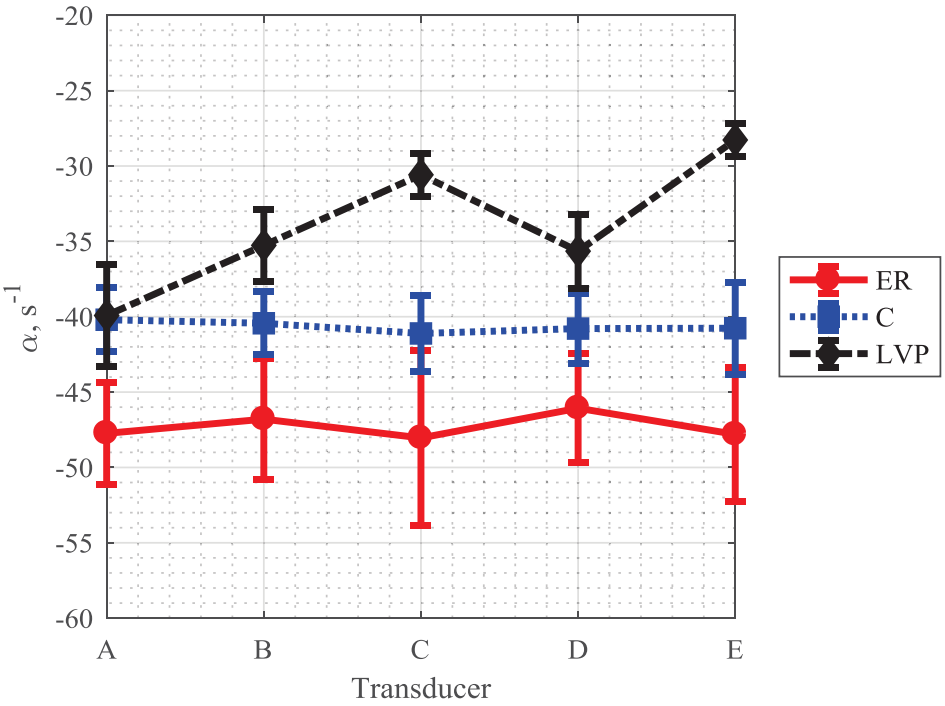


**Figure 6.12.** 1T Decay Rates

Significantly more confidence can be attributed to the trend presented in this manuscript. The overarching result was, in order of most damping to least damping:

1. The equal-radius-of-curvature nozzle
2. The conical nozzle
3. The linear-velocity-profile nozzle

This is a useful result to apply towards the development of nozzles on systems that tend towards experiencing a prominent 1T instability, as any mitigation is useful. Of course, these results were without mean-flow, and hence they do not explicitly represent the acoustics that should be expected in actual flight. The primary difference, neglecting the influence of combustion, arises from the lack of a sonic surface at the throat, which prohibits the propagation of acoustic phenomena upstream. This would primarily influence longitudinal modes, or mixed modes with a longitudinal component far stronger than pure

transverse modes. However, that is not to say that there would be no difference between this experiment and one that utilized mean flow.

Without simulations, it is difficult to ascertain the mechanism behind the geometric trend in damping. In Price, et al. **[60]**, reasoning involving the normal vectors of the converging sections was applied to explain the resulting trend. In light of the shift in the trend reported in this work, the previous reasoning is now erroneous. It is likely that the means in which the waves reflect are the primary mechanism behind the trend in damping, but any attempt to describe the physics involves significant speculation at this stage.

# CHAPTER SEVEN
# CONCLUSIONS AND FUTURE WORK

To examine the damping of transverse modes, an experiment was carried out involving three nozzles with an equal-radius-of-curvature nozzle, a conical nozzle, and a linear-velocity-profile nozzle. These nozzles resembled nozzles previously tested under 1L excitation **[1, 2]**. Due to experimental and temporal limitations, the scope of the experiment was reduced from analyzing the 1L, 1T1L, 1T, and 1R mode under both no mean-flow and under mean flow to an experiment involving the 1T1L and 1T mode under no mean-flow conditions. An inability to produce consistent results forced 1T1L efforts to be abandoned in favor of the 1T, which was viewed as more important and relevant.

1T data were taken from six transducers arranged in a tangential configuration and sampled at 40 kHz. The appropriate frequency for the 1T mode was identified as 1500 Hz in each nozzle, and the necessary means for attenuation testing was provided by a 3D printed, spring-activated gate-valve. This fast-acting valve served to eliminate the flow of oscillatory flow to the test geometries, and the resulting decay of the excited mode was captured. The natural log of the upper envelope of the pressure trace filtered by a $2^{nd}$ order Butterworth filter were used to apply linear fits in a computed decay window. The slope of these linear fits corresponded to the decay rate of the exponential decay of the resonant mode, and these data were used to ascertain the damping characteristics of the three nozzles. Under these conditions, it was shown that the ER nozzle provided the most 1T damping, followed by the conical nozzle, which was followed by the LVP nozzle.

The possibility for expansion in this work is *extensive*. Obviously, the inclusion of mean flow for all nozzles is the first logical step in expanding the scope of this work. It would be of interest to observe if the same trend captured under no mean flow similarly emerges in the presence of mean flow, or if the acoustics are so different a new result is found. Another room for expansion would be to modify the experiment such that 1T1L data can be reliably obtained—this would not be a difficult expansion, and would at most require a modification to the air-delivery system from the siren to accommodate the necessary rotation of the chambers. This may also be avoided by injecting the oscillatory

flow from the head-end of the chamber, though it would remain to be seen if the reduction in magnitude observed when driving in this scheme would preclude data acquisition.

Driving the 1L and 1R modes would require greater modification to the current experiment. Both would require an acoustic driver capable of producing a discrete signal at both low and high frequencies, which is something the current driver—a pneumatic siren—was unable to accomplish. However, supposing that such a driver was found, the methodology presented in this work could easily be extended to analyze these modes.

# BIBLIOGRAPHY

[1] Janardan, B. A., Daniel, B. R., and Zinn, B. T., "Damping of Axial Instabilities by Small-Scale Nozzles Under Cold-Flow Conditions," *Journal of Spacecraft and Rockets* Vol. 11, No. 12, Dec. 1974, pp. 812-820.

[2] Janardan, B. A., "Damping of Axial Instabilities by Solid Propellant Rocket Exhaust Nozzles," Ph.D. Dissertation, School of Aerospace Engineering, Georgia Institute of Technology, Atlanta, GA., August 1973.

[3] Kathan, R., Morgenweck, D., Kaess, R., and Sattelmayer, T., "Validation of the Computation of Rocket Nozzle Admittances with Linearized Euler Equations," *Progress in Propulsion Physics* Vol. 4, 2013, pp. 135-148.

[4] Shipley, K., Morgan, C., and Anderson, W. E., "Computational and Experimental Investigation of Transverse Combustion Instabilities," AIAA Paper 2013-3992, July 2013.

[5] Flandro, G. A., Majdalani, J., and Sims, J. D., "On Nonlinear Combustion Instability in Liquid Propellant Rocket Engines," AIAA Paper 2004-3516, July 2004.

[6] Bibik, O., Lubarsky, E., Shcherbik, D., Hadjipanayis, M, and Zinn, B. T., "Rotational Traveling of Tangential Wave in Multi-Injectors LRE Combustion Simulator," AIAA Paper 2008-1001, January 2008.

[7] Jacob, E. J., "A Study of Nonlinear Combustion Instability," Ph.D Dissertation, Dept. of Mechanical Aerospace and Biomedical Engineering, University of Tennessee, Knoxville, TN, 2009.

[8] Shimizu, T., Morii, Y., and Daimon, Y., "An Order Estimation of the Acoustic Losses Inside a Simulated Liquid Rocket Chamber," AIAA Paper 2013-4061, July 2013.

[9] Cantrell, R. H., and Hart, R. W., "Interaction Between Sound and Flow in Acoustic Cavities: Mass, Momentum, and Energy Considerations," *Journal of The Acoustical Society of America* Vol. 36, No. 4, April 1964, pp. 679-706.

[10] Javed, A., and Chakraborty, D., "Damping Coefficient prediction of Solid Rocket Moter Nozzle using Computational Fluid Dynamics," *Journal of Propulsion and Power* Vol. 30, No. 1, Jan.-Feb. 2014, pp. 19-23.

[11] Price, E. W., "Experimental Solid Rocket Combustion Stability," *Tenth Symposium (International) on Combustion*, The Combustion Institute, Pittsburgh, Pa., 1965, pp.1067-1082.

[12] Blomshield, F. S., Mathes, H. B., Crump, J. E., Beiter, C. A., and Beckstead, M. W., "Nonlinear Stability Testing of Full-Scale Tactical Motors," *Journal of Propulsion and Power* Vol. 13, No. 3, May-June 1997, pp. 356-366.

[13] Culick, F. E. C., and Dehority, G. L., "Analysis of Acoustic Waves in a Cold-Flow Rocket," *Journal of Spacecraft and Rockets* Vol. 6, No. 5, May 1969, pp. 591-595.

[14] Oefelein, J. C., and Yang, V., "Comprehensive Review of Liquid-Propellant Combustion Instabilities in F-1 Engines," *Journal of Propulsion and Power* Vol. 9, No. 5, Sept-Oct. 1993, pp. 657-676.

[15] Sigman, R. K., and Zinn, B. T., "A Finite Element Approach for Predicting Nozzle Admittances," *Journal of Sound and Vibration* Vol. 88, No. 1, 1983, pp. 117-131.

[16] Jacob, E. J., "Preliminary Results Concerning Nonlinear Acoustic Damping in a Forced Rijke Tube," AIAA Paper 2013-0757, Jan. 2013.

[17] French, J. C., "Nozzle Acoustic Dynamics and Stability Modeling," *Journal of Propulsion and Power* Vol. 27, No. 6, Nov.-Dec. 2011, pp. 1266-1275.

[18] Blomshield, F. S., "Lessons Learned in Solid Rocket Combustion Instability," AIAA Paper 2007-5803, July 2007.

[19] French, J. C., Flandro, G. A., Gloyer, P. W., and Jacob, E. J., "UCDS Nozzle Acoustic Dynamics and Stability Modeling," AIAA Paper 2010-6994, July 2010.

[20] Zinn, B. T., "Longitudinal Mode Acoustic Losses in Short Nozzles," *Journal of Sound and Vibration* Vol. 22, No. 1, 1972, pp. 93-105.

[21] Buffum, F. G. J., Dehority, G. L., Slates, R. O., and Price, E. W., "Acoustic Attenuation Experiments on Subscale, Cold-Flow Rocket Motors," *AIAA Journal* Vol. 5, No. 2, January 1966, pp. 272-280.

[22] Zinn, B. T., "Review of Nozzle Damping in Solid Rocket Instabilities," AIAA Paper 72-1050, Nov.-Dec. 1972.

[23] Blomshield, F. S., Mathes, H. B., Crump, J. E., Stalnaker, R. A., and Beckstead, M. W., "Stability Testing of Full-Scale Tactical Motors," *Journal of Propulsion and Power* Vol. 13, No. 3, May-June 1997, pp. 349-355.

[24] Anderson, J. D., *Modern Compressible Flow with Historical Perspective*, 3rd ed., McGraw Hill, New York, 2003.

[25] Pierce, A. D., *Acoustics: An Introduction to its Physical Principles and Applications*, Acoustical Society of America, Melville, NY., 1989.

[26] Randall, R. H., *An Introduction to Acoustics*, Dover Publications, New York, 2005.

[27] Nagle, R. K., Saff, E. B., and Snider, A. D., *Fundamentals of Differential Equations*, 8th ed., Pearson Education, Inc., Boston, MA., 2012.

[28] Palm, W. J. I., *System Dynamics*, 3rd Ed., McGraw Hill, New York, NY., 2014.

[29] Gray, G. L., Costanzo, F., and Plesha, M. E., *Engineering Mechanics: Dynamics*, 2nd Ed., McGraw Hill, New York, NY., 2013.

[30] Haberman, R., *Applied Partial Differential Equations with Fourier Series and Boundary Value Problems*, 4th ed., PEARSON EDUCATION, INC., Upper Saddle River, New Jersey, 2004.

[31] Natanzon, M. S., *Combustion Instability*, edited by Culick, F. E. C., 222, Progress in Astronautics and Aeronautics, AIAA, New York, 1999.

[32] Wilson, A. W., Flandro, G. A., and Jacob, E., "Steepened Tangential Waves: DC Offset and Pressure "Valleys"," AIAA Paper 2014-3488, July 2014.

[33] Wieber, P. R., "Acoustic Decay Coefficients of Simulated Rocket Combustors," NASA TN D-3425, May 1966.

[34] Quinlan, J. M., and Zinn, B. T., "Transverse Combustion Instabilities: Modern Experimental Techniques and Analysis," AIAA Paper 2014-3682, July 2014.

[35] Sirignano, W. A., and Popov, P., "Two-Dimensional Model for Liquid-Rocket Transverse Combustion Instability," AIAA Paper 2013-0566, January 2013.

[36] Staschus, C. I., and Frederick, R. A. Jr., "An Overview of Combustion Instabilities and Rocket Engine Injector Design," AIAA Paper 2016-4724, July 2016.

[37] Zinn, B. T., Bell, W. A., Daniel, B. R., and Smith, A. J. Jr., "Experimental Determination of Three Dimensional Liquid Rocket Nozzle Admittances," AIAA Paper 72-666, June 1972.

[38] Fiala, T., Kathan, R., and Sattelmayer, T., "Effective Stability Analysis of Liquid Rocket combustion Chambers: Experimental Investigation of Damped Admittances," International Astronautical Fedaration Paper IAC11-C4.3.11, Paris., 2011.

[39] Nguyen, T. M., Popov, P. P., and Sirignano, W. A., "Driving Mechanisms of Liquid-Propellant Rocket Longitudinal Combustion Instability," AIAA Paper 2017-0822, January 2017.

[40] Hart, R. W., and McClure, F. T., "Theory of Acoustic Instability in Solid Propellant Rocket Combustion," Tenth Symposium (International) on Combustion, 1964.

[41] Yang, V., Yoon, M. W., and Wicker, J. M., "Acoustic Waves in Baffled Liquid-Propellant Rocket Engines," ADA267260, Air Force Office of Scientific Research, Bolling AFB, D.C., May 1993.

[42] Sutton, G. P., and Biblarz, O., *Rocket Propulsion Elements*, 8th, John Wiley & Sons, Inc., Hoboken, NJ., 2010.

[43] French, J. C., "Analytic Evaluation of a Tangential Mode Instability in a Solid Rocket Motor," AIAA Paper 2000-2689, July 2000.

[44] Weidong, L., Zhenguo, W., Jin, Z., and Fengchen, Z., "Numerical Analysis Model for Radial Combustion Instability of Liquid Propellant Engine," AIAA Paper 1997-3327, 1997.

[45] Jourdain, G., Eriksson, L., Kim, S. H., and Sohn, C. H., "Application of Dynamic Mode Decomposition to Acoustic-Modes Identification and Damping in a 3-Dimensional Chamber with Baffled Injectors," *Journal of Sound and Vibration* Vol. 332, February 2013, pp. 4308-4323.

[46] Dehority, G. L., "Resume of Nozzle Damping Theory," ADA063466, Naval Weapons Center, China Lack, CA, 1979.

[47] Bell, W. A., "Experimental Determination of Three-Dimensional Liquid Rocket Nozzle Admittances," Ph.D. Dissertation, School of Aerospace Engineering, Georgia Institute of Technology, Atlanta, GA., July 1972.

[48] Crocco, L., and Sirignano, W. A., "Behavior of Supercritical Nozzles under Three-Dimensional Oscillatory Conditions," Advisory Report 117, AGARD, 1967.

[49] Sun, B., Li, J., Su, W., and Wang, N., "Study on the Effects of Gas Temperature on Cold Flow Test of Nozzle Damping," AIAA Paper 2015-3790, July 2015.

[50] Bell, W. A., and Zinn, B. T., "The Prediction of Three-Dimensional Liquid-Propellant Rocket Nozzle Admittances," NASA CR-121129, February 1973.

[51] Marble, F. E., and Candel, S. M., "Acoustic Disturbance From Gas Non-Uniformities Convected Through a Nozzle," *Journal of Sound and Vibration* Vol. 55, No. 2, 1977, pp. 225-243.

[52] Crocco, L., Monti, R., and Grey, J., "Verification of Nozzle Admittance Theory by Direct Measurement of the Admittance Parameter," *ARS Journal* Vol. 31, No. 6, 1961, pp. 771-775.

[53] Su, W., Wang, N., Li, J., Zhao, Y., and Yan, M., "Numerical Research on the Nozzle Damping Effect by a Wave Attenuation Method," *Journal of Defense Technology* Vol. 9, Oct. 2013, pp. 162-166.

[54] Janardan, B. A., and Zinn, B. T., "Rocket Nozzle Damping Characteristics Measured Using Different Experimental Techniques," *AIAA Journal* Vol. 15, No. 3, 1976, pp. 442-444.

[55] Melling, T. H., "An Impedance Tube for Precision Measurement of Acoustic Impedance and Insertion Loss at High Sound Pressure Levels," *Journal of Sound and Vibration* Vol. 28, No. 1, 1973, pp. 23-54.

[56] Kathan, R., and Sattelmayer, T., "Investigation of Damping Mechanisms in a Cold Flow Rocket Combustion Chamber," EOARD, London, Great Britain, June 2011.

[57] Sattelmayer, T., Kathan, R., Kóglmeier, S., Kaess, R., and Nicole, A., "Validation of Transverse Instability Damping Computations for Rocket Engines," *Journal of Propulsion and Power* Vol. 31, No. 4, July-Aug. 2015, pp. 1148-1157.

[58] Schulze, M., Kathan, R., and Sattelmayer, T., "Impact of Absorber Ring Position on Cavity Length and Acoustic Damping," *Journal of Spacecraft and Rockets* Vol. 52, No. 3, May-June 2015, pp. 917-927.

[59] ""Smooth Cast 385"," Smooth-On [company website], https://www.smooth-on.com/products/smooth-cast-385/ [cited 5-29-2017].

[60] Price, T. J., Moeller, T. M., Cranford, J. T., Batterson, J. W., and Jacob, E. J., "Experimental Investigation of Transverse Mode Nozzle Damping: Preliminary Results," AIAA Paper 2017-5131, Sept. 2017.

# VITA

Theron J. Price was born and raised in Morristown, TN. He obtained his Bachelor of Science in Aerospace Engineering from the University of Tennessee, Knoxville, in May 2015. Immediately after, he accepted a graduate research assistantship at the University of Tennessee Space Institute under Dr. Trevor M. Moeller, and received his Master of Science degree in December 2017.